J. Fluid Mech. (2001), *vol.* 427, *pp.* 73–105. Printed in the United Kingdom

© 2001 Cambridge University Press

Splash formation by spherical drops

By LIOW JONG LENG

GK Williams Cooperative Research Centre for Extractive Metallurgy,
Department of Chemical Engineering, The University of Melbourne, Parkville,
Victoria, Australia 3052

(Received 27 November 1998 and in revised form 10 July 2000)

The impact of a spherical water drop onto a water surface has been studied experimentally with the aid of a 35 mm drum camera giving high-resolution images that provided qualitative and quantitative data on the phenomena. Scaling laws for the time to reach maximum cavity sizes have been derived and provide a good fit to the experimental results. Transitions between the regimes for coalescence-only, the formation of a high-speed jet and bubble entrapment have been delineated. The high-speed jet was found to occur without bubble entrapment. This was caused by the rapid retraction of the trough formed by a capillary wave converging to the centre of the cavity base. The converging capillary wave has a profile similar to a Crapper wave. A plot showing the different regimes of cavity and impact drop behaviour in the Weber–Froude number-plane has been constructed for Fr and We less than 1000.

1. Introduction

The impact of a liquid drop onto the surface of another liquid has been studied for many years and pictures of the event make striking visual images (Worthington 1908; Edgerton & Killian 1954). There is a wide range of phenomena associated with, and subsequent to, drop impact resulting in an extensive literature (Engel 1967; Pumphrey & Elmore 1990; Oğuz & Prosperetti (1990, hereafter referred to as OP(I)); Rein 1996; Morton, Rudman & Liow 2000). Nevertheless a map of the phenomena observed as a function of the controlling dimensionless parameters is far from complete. The splash associated with the impact of a liquid drop is of interest in metallurgical processes (Liow *et al.* 1995; Liow & Gray 1996) as it provides a basic understanding of a wide variety of processes that can form a splash. The processes include the injection of solid particles into a melt, sloshing of melt during gas injection or transportation, venting of gas injected into melts, casting of metals, and spray coating with liquid metals. Apart from metallurgical applications, splash dynamics is important in the erosion of soil, spreading of pathogens, impact of meteorites, impact of raindrops, and competitive sports (Morton *et al.* 2000).

For liquids with low viscosities such as ethanol or water, the impact of a liquid drop involves a number of phenomena which are primarily determined by the Weber ($We = \rho u^2 d/\sigma$) and Froude ($Fr = u^2/gd$) numbers where ρ is the drop density, u its velocity, d its diameter, σ the surface tension and g is the acceleration due to gravity. At very low impact velocities, the impinging drop has been observed to coalesce with the bulk liquid but may also bounce or float (Rodriguez & Mesler 1985). Cresswell & Morton (1995) showed that during the initial stages of impact, the target liquid rises up the impacting drop. Capillary waves are propagated up the impacting drop as well as away from the impact site. A small cavity is formed and a wave swell

https://doi.org/10.1017/S0022112000002500 Published online by Cambridge University Press

appears at the edge of the cavity. The cavity collapses with more capillary waves propagating outwards. As the impact velocity increases, the cavity collapses to form a central jet with splash droplets. A vortex ring, first studied in detail by Chapman & Critchlow (1967), is formed and travels into the bulk liquid; the depth of travel depends on the impact velocity. Rodriguez & Mesler (1985) suggested that drops that splash do not form vortex rings and showed that a boundary between splashing and vortex ring formation occurred at a Reynolds number near 3000 for Froude numbers ranging from 16 to 400. Hsiao, Lichter & Quintero (1988), using their own data for mercury drops (Reynolds number of 20 000) and that of Rodriguez & Mesler (1985), suggested that an upper limit to the formation of vortex rings that follows drop impact is a Weber number of 64 and not dependent on the Reynolds number. Cresswell & Morton (1995) argued that the boundary condition on the viscous stress at the free surface is sufficient to account for enough vorticity to result in vortex ring formation. As the Weber number does not include viscosity, Cresswell & Morton used a force balance between the surface tension and pressure generated by drop impact and obtained a value for the upper limit of the Weber number.

In a series of experiments on 2.3 mm diameter water drops, Rein (1996) found that the transition between coalescence and splashing proceeds through a regime where a thick central jet is formed followed by a regime where bubble entrapment coupled with a thin high-speed jet is observed. Rein noticed that the entrapment of bubbles did not always accompany the formation of the thin high-speed jet and concluded that small disturbances acted to suppress bubble entrapment. Pumphrey & Elmore (1990) showed that the bubble entrapment regime had an upper and lower boundary on the (We, Fr)-plane. OP(I) argued that the upper limit was a balance between the even spread of the drop over the surface of a hemispherical cavity and a surface tension restoring force. They obtained $We \sim Fr^{1/4}$ which fitted the experimental data of Pumphrey & Elmore (1990). Pumphrey & Elmore (1990) observed 'a capillary wave which travels down the sides of the crater. When this wave reaches the bottom of the crater, its crest closes in from all sides, thus trapping the bubble'. OP(I) argued that 'Whether a bubble is entrapped or not is determined by a delicate balance between the times at which the outward motion of the crater walls is reversed at different positions'. They reasoned that the time to maximum growth of the crater scales proportionally to drop diameter times the drop velocity to the third power, based on experimental observation by Pumphrey (privately communicated to OP(I)). Relating this to the time for a capillary wave formed at the bottom of the cavity to reverse its motion, they obtain the lower limit for bubble entrapment as $We \sim Fr^{1/5}$. Although the relationship fitted the experimental results well, their boundary integral simulation of the bubble entrapment for drops falling at terminal velocity indicated that the bubble entrapment envelope was larger than that found from the experimental results (Oğuz & Prosperetti 1991).

The regime above the bubble entrapment regime is characterized by cavity collapse to form a thick jet where one or two large drops are detached with a low velocity and the sides of the cavity form a crown which breaks up to form small splash drops (Worthington 1908; Edgerton & Killian 1954). At even higher velocities (Engel 1966), the cavity formed is hemispherical in shape and the crown that develops rises high enough to lose its momentum so that surface tension pulls it inwards to form a canopy over the cavity. This canopy meets at the centre and a weak jet is ejected upwards and a stronger jet ejected downwards. The downward jet halts the rise of the thick central jet formed from the cavity collapse. The central jet normally does not break through the canopy.

https://doi.org/10.1017/S0022112000002500 Published online by Cambridge University Press

The condition for the start of the splashing regime has not been defined. Highly accurate data covering the region of interest are not available because most of the experiments used 16 mm film which has limited resolution. The present study, in particular, attempts to provide more accurate quantitative data so that the transition between different regimes can be characterized accurately and conflicting theories resolved. The important parameters governing cavity dynamics are obtained from photographic evidence enabling scaling laws to be derived for cavity growth and collapse. The different regimes of the splashing phenomena identified are identified on a We, Fr diagram for Fr and We less than 1000 for water drops impacting on water.

2. Experimental

The impact behaviour was mapped by releasing water drops from different heights into a glass tank 200 mm square and 100 mm deep, in order to vary the drop impact velocity. The tank was filled with distilled water to the brim to reduce surface tension effects on the tank edges. Successive runs were carried out quickly and the water was changed between each set of runs to minimize the effects of surface impurities. A video system was used to map the drop heights where substantial changes in drop impact behaviour could be observed. Initially, a 16 mm Hycam was used to photograph drop impact but it was found that the frame size (10.05×7.42 mm) and film type available limited the details that could be seen (Morton *et al.* 2000).

A 35 mm drum camera was constructed with a maximum framing rate of 3 kHz (Lawson & Liow 1998). A 1880 mm length of 35 mm film was secured around a 600 mm diameter drum to give 152 frames $\frac{1}{3}$ the size of a standard 35 mm film frame which provided about four times more area than a frame of the 16 mm film. Kodak TMAX400 film with a resolution of 110 lines/mm was used and push processed with TMAX developer to ASA1600. A 1kHz EG&G Model MVS-2613 strobe with a maximum pulse energy of 40 mJ and a pulse duration of 5 μs was used to illuminate the object area. A 105 mm Micro Nikor lens was used at f11 to f16 to image the drop. The strobe frequency and number of pulses were controlled through a variable frequency generator and a Stanford Research Systems DG535 timing box (maximum trigger delay of 85 ns). A He–Ne laser beam focused onto a photodiode was placed in the path of the drop. When the drop traversed the laser beam, a signal was sent to the timing box which delayed the first strobe pulse to synchronize with the drop impact. Two 5×5 mm (±0.01 mm) squares (0.5 mm thick), one placed above and the other below the water surface, were used to provide a scale for measurements. The velocity and diameter of the drop before impact is accurate to ±1.5%. The accuracy of the frequency generator is ±0.1% and measured by an oscilloscope prior to each experiment. The length is scaled by the drop diameter, d, and time by d/u, where u is the drop velocity.

2.1. *Drop formation*

In the early works on drop impact, drops were usually formed from the tip of a burette. Drops produced from a burette, even with its tip ground flat, were found to be asymmetrical, skewed and oscillating in all three dimensions. Video footage of the impact showed that a large number of drops did not impact normally to the water surface and the splash events were not repeatable. A survey of the literature showed that the drops of Rodriguez & Mesler (1988, figure 2) exhibited considerable

https://doi.org/10.1017/S0022112000002500 Published online by Cambridge University Press

skewness. Therefore, it can be expected that most experiments using a burette for drop formation are not easily repeatable.

To overcome the effect of the drop skewness and oscillation, smaller drops were required and hypodermic needles with their tips ground flat were used. Wood's metal was solidified around the needle to provide body for grinding. A 33 gauge (0.203 mm [$\pm$0.001 mm] external diameter) and a 16 gauge needle (1.645 mm [$\pm$0.001 mm] external diameter) were used. The needle was attached to a travelling vernier ($\pm$0.01 mm accuracy) and the height of fall was measured from the needle tip to the water surface. All runs with spherical drops were carried out with the 33 gauge (33G) needle because the larger needle size gave larger drops that were not spherical at impact. Runs from the 16G needle were used only to provide a second set of data to delineate the region of bubble entrapment. This preparation of the needles gave repeatable results with the drop impacting normally to the water surface. To check repeatability, the strobe was flashed once at a predetermined delay and the image captured on video. This was repeated a number of times allowing different drops to be compared. The repeatability of the cavity formation is within 0.2 ms, the jet formation to 0.5 ms, the collapse of the jet back into the water bath to 2 ms.

The 35 mm photographs were digitized with a Polaroid Sprintscan at 2700 dpi (106 dpmm) to obtain quantitative data. The drop diameter remained constant with each needle size. Drops produced by the 33G needle were around 2.1 mm in diameter and were spherical at impact to within 1.5% (one pixel resolution or 30 microns when digitized) while the 16G needle gave drops that oscillated throughout the range of fall heights used. Higher-resolution pictures of the 33G needle drops indicated that they were spherical to 1.0%. Keeping the drop diameter constant and changing the height of fall only changes the impact velocity, giving a constant Bond number ($Bo = We/Fr$) for a fixed drop size. The Weber and Froude numbers could be determined to an accuracy of $\pm$2%. The data were spaced out evenly to cover the regime of coalescence, primary bubble entrapment and beyond as shown in figure 1. However, the region where the crown rises and closes on itself was not reached due to limitations on the height achievable with the travelling vernier. The minimum drop height of 80 mm was limited by the size of the drop detector unit positioned below the needle and the measurement scale. The density of water, measured with a density bottle, was 998 kg m^{-3}. The surface tension, measured by the pendant drop method, using an FTA200 instrument by FTA Corp., was 71×10^{-3} Nm^{-1}.

From the digitized images, the drop velocity, cavity depth and cavity width were obtained. The cavity width was measured as close as possible to the undisturbed free surface; the vertical position is fixed for each case and within 0.5 mm of the undisturbed free surface (the measurement squares providing the reference point). A ratio e is defined as the cavity width divided by twice the cavity depth with a value of 1 for a hemispherical cavity, < 1 for a prolate cavity and > 1 for an oblate cavity.

3. Cavity formation and collapse

In the formation and collapse process the cavity varies from a smooth shape at low Fr and We to one with sharp angular corners and a highly disturbed wave swell at high Fr and We. The wave swell is defined here as the rim of the impact cavity that is initially intact and subsequently spreads radially outwards. A selection of experimental data across the range collected showing the cavity formation and collapse shapes is given in figure 2. In this section, the behaviour of the cavity as

https://doi.org/10.1017/S0022112000002500 Published online by Cambridge University Press

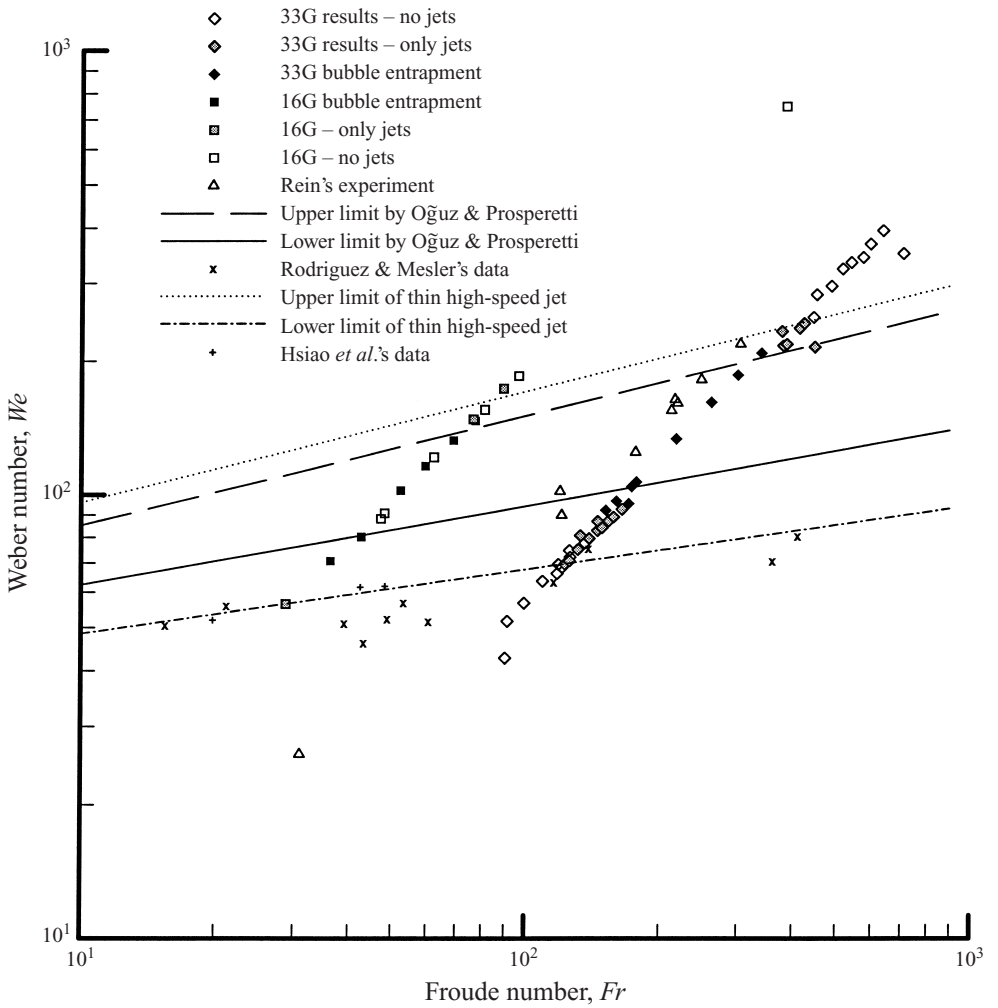


FIGURE 1. Each experimental run corresponds to a point on the Weber–Froude number plane. Two drop sizes from a 16G and 33G needle were used to traverse the high-speed jet and bubble entrapment regimes. The experimental error bar is of the size of the symbols used and thus omitted. Rein's experimental runs are included for comparison. The lines Oğuz & Properetti mark the boundaries of the bubble entrapment regime and the dash-dotted and dotted lines are the lower and upper limit for the thin high-speed jet formation found in this study. Rodriguez & Mesler's and Hsiao *et al.*'s data are for cases that fall on the vortex ring–splash boundary.

observed experimentally is presented and discussed beginning at the low *Fr* and *We* and progressing to the higher values.

3.1. *Coalescence regime*

At low *We* and *Fr*, the drop may coalesce, float or bounce after impact. During coalescence, it is known that a thin film of the target liquid rises up the drop faster than the drop merges with the target fluid. As the drop continues its downward motion a smooth capillary wave front moves outwards. The flat tops seen in figures 2(*a*) and 2(*b*) indicate that the radial wave is axisymmetric. The front of the wave initially has a steep angle which falls rapidly as the wave front moves out.

https://doi.org/10.1017/S0022112000002500 Published online by Cambridge University Press

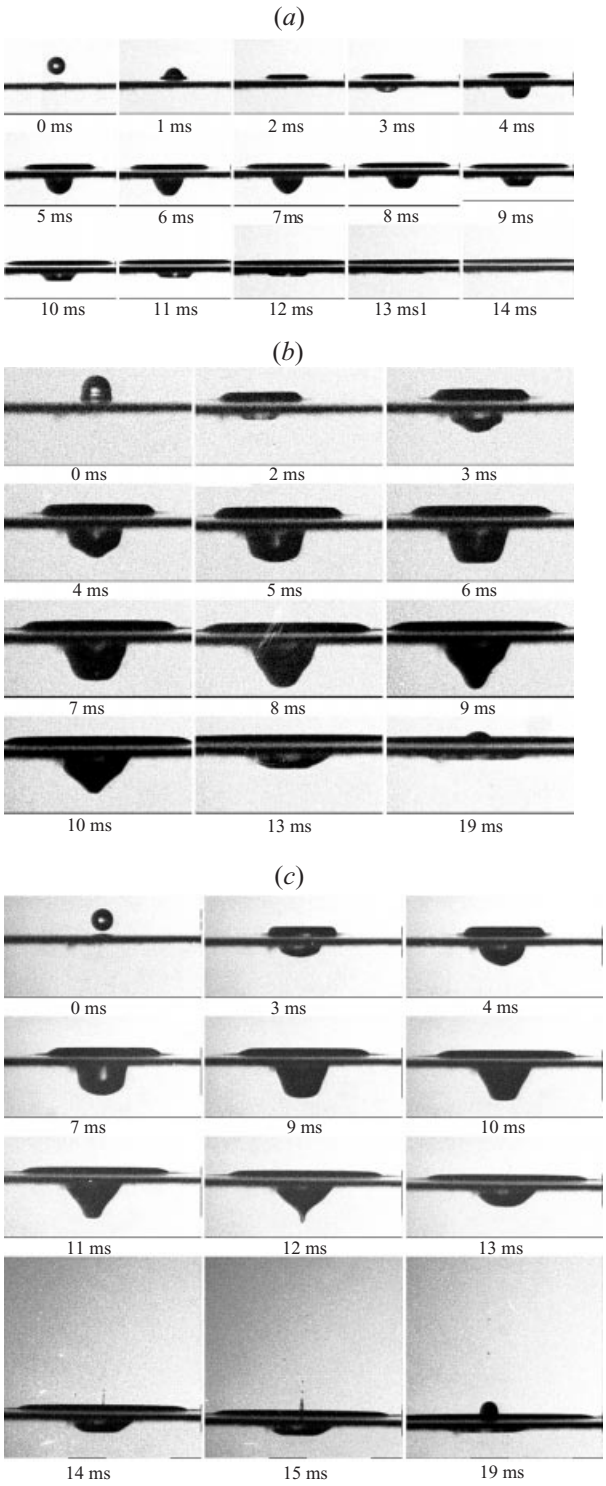


FIGURE 2(*a–c*). For caption see page 81.

https://doi.org/10.1017/S0022112000002500 Published online by Cambridge University Press

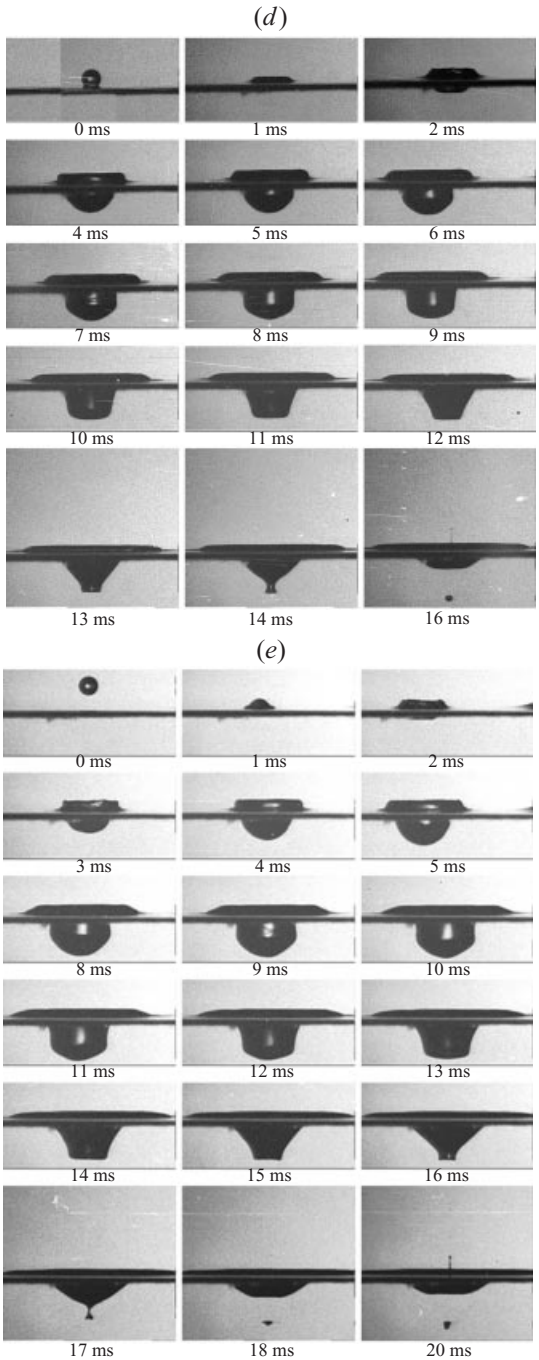


FIGURE 2(*d*,*e*). For caption see page 81.

The cavity formed at these low *Fr* and *We* survives for only a short time. Figure 2(*b*) shows a sequence for $Fr = 119$ and $We = 70$. The cavity shapes at these low values are not smooth: they are initally oblate in shape and the base grows downwards to form a sharp point. From the sides of the cavity, a sharp corner is

https://doi.org/10.1017/S0022112000002500 Published online by Cambridge University Press

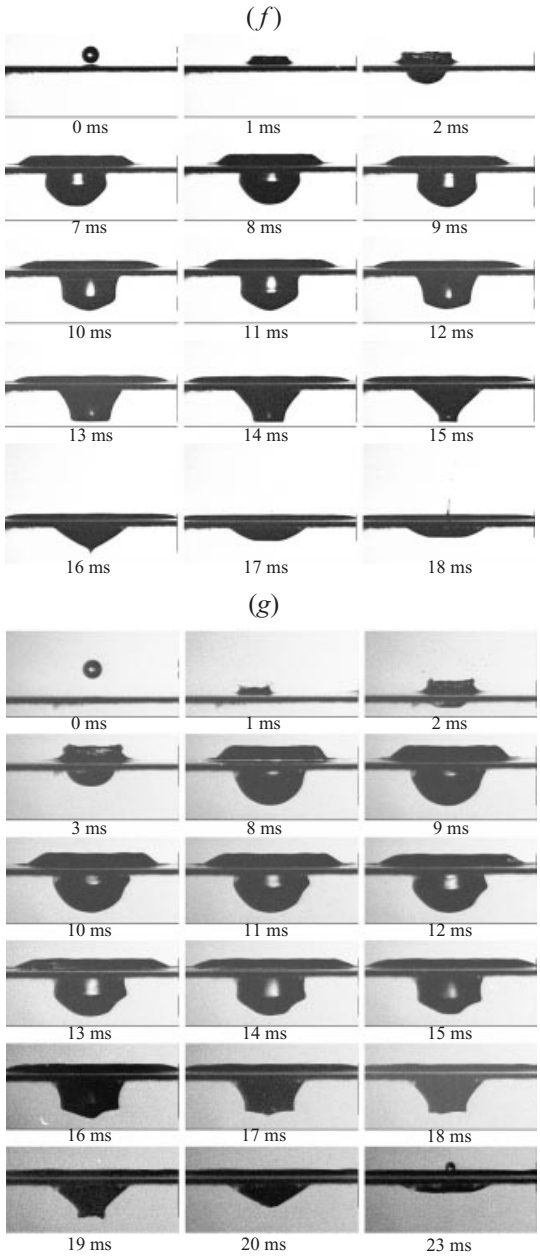


FIGURE 2(*f*,*g*). For caption see page 81.

seen moving downwards. At 5 ms after impact, the growth of the cavity centre slows down (see dimensionless depth R' at dimensionless time $t' = 3$ in figure 3) and the corner has approached the same depth as the base of the cavity. A flat cavity bottom is seen 6–7 ms after impact. From the corner a capillary wave converges to the cavity centreline. The capillary wave profiles become increasingly rounded with time and the base at the cavity centre is forced downwards. The increase in R' can be seen at $t' = 7$ in figure 3. Surface tension acts against the deformation and causes the

https://doi.org/10.1017/S0022112000002500 Published online by Cambridge University Press

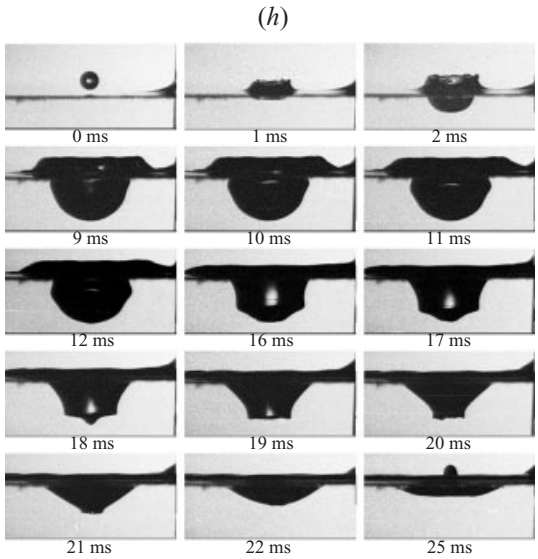


FIGURE 2. The formation and collapse of the cavity over the range of *We* and *Fr* studied. (*a*) $Fr = 90$, $We = 43$, $d = 1.86$ mm and $u = 1.29\,\mathrm{m\,s^{-1}}$. (*b*) $Fr = 119$, $We = 70$, $d = 2.07$ mm and $u = 1.56\,\mathrm{m\,s^{-1}}$. (*c*) $Fr = 146$, $We = 87$, $d = 2.09$ mm and $u = 1.73\,\mathrm{m\,s^{-1}}$. (*d*) $Fr = 219$, $We = 134$, $d = 2.12$ mm and $u = 2.13\,\mathrm{m\,s^{-1}}$. (*e*) $Fr = 301$, $We = 186$, $d = 2.13$ mm and $u = 2.51\,\mathrm{m\,s^{-1}}$. (*f*) $Fr = 449$, $We = 216$, $d = 1.88$ mm and $u = 2.88\,\mathrm{m\,s^{-1}}$. (*g*) $Fr = 454$, $We = 283$, $d = 2.14$ mm and $u = 3.09\,\mathrm{m\,s^{-1}}$. (*h*) $Fr = 543$, $We = 335$, $d = 2.13$ mm and $u = 3.37\,\mathrm{m\,s^{-1}}$.

cavity base to rise up and arrest the inwards growth of the capillary wave. The time between the two successive formations of a sharp point at the cavity base is around 4–5 ms and the height of the capillary wave is approximately equivalent to the drop diameter. For a 2.1 mm diameter drop, the oscillation period of a spherical drop is $\sqrt{3\pi\rho V/(n(n-1)(n+2)\sigma)}$. The periods corresponding to $n = 2$, 3 and 4 are 8.97, 4.63 and 2.99 ms respectively. The period of a capillary wave with the wavelength of the drop diameter of 2.1 mm is 4.5 ms and is comparable to the time in the experiment between the cavity base forming sharp points. The time to reach maximum cavity depth is 9 ms or twice that of the capillary wave period or one oscillation period of a spherical drop with $n = 2$.

Figure 3 shows the variation of the *e* ratio and dimensionless cavity depth (R') with dimensionless time for drop impacts in this regime. The growth phase of the cavity for the first three dimensionless time units falls on the same dimensionless curve. The cavity grows with its base moving down rapidly while its diameter at the position of the original undisturbed interface expands more slowly. The cavity is prolate in shape with width comparable to the depth for most of the growth phase. The prolate shape gives the cavity base a smaller radius of curvature than it would attain if it grew hemispherically. The rate of collapse of the cavity increases with *Fr* and *We*. The base of the prolate shaped cavity flattens out as it collapses. This flattening happens rapidly at the start but slows down with time due to the converging capillary wave. The rapid initial cavity collapse gives a rapid change in the sign of the curvature at the cavity base and has been shown by Rodriguez & Mesler (1988) and Rein (1996) to initiate vortex ring detachment. A central jet is just barely visible. It rises less than 0.2 dimensionless lengths above the free surface of the outward travelling waves and collapses within 8–10 ms.

https://doi.org/10.1017/S0022112000002500 Published online by Cambridge University Press

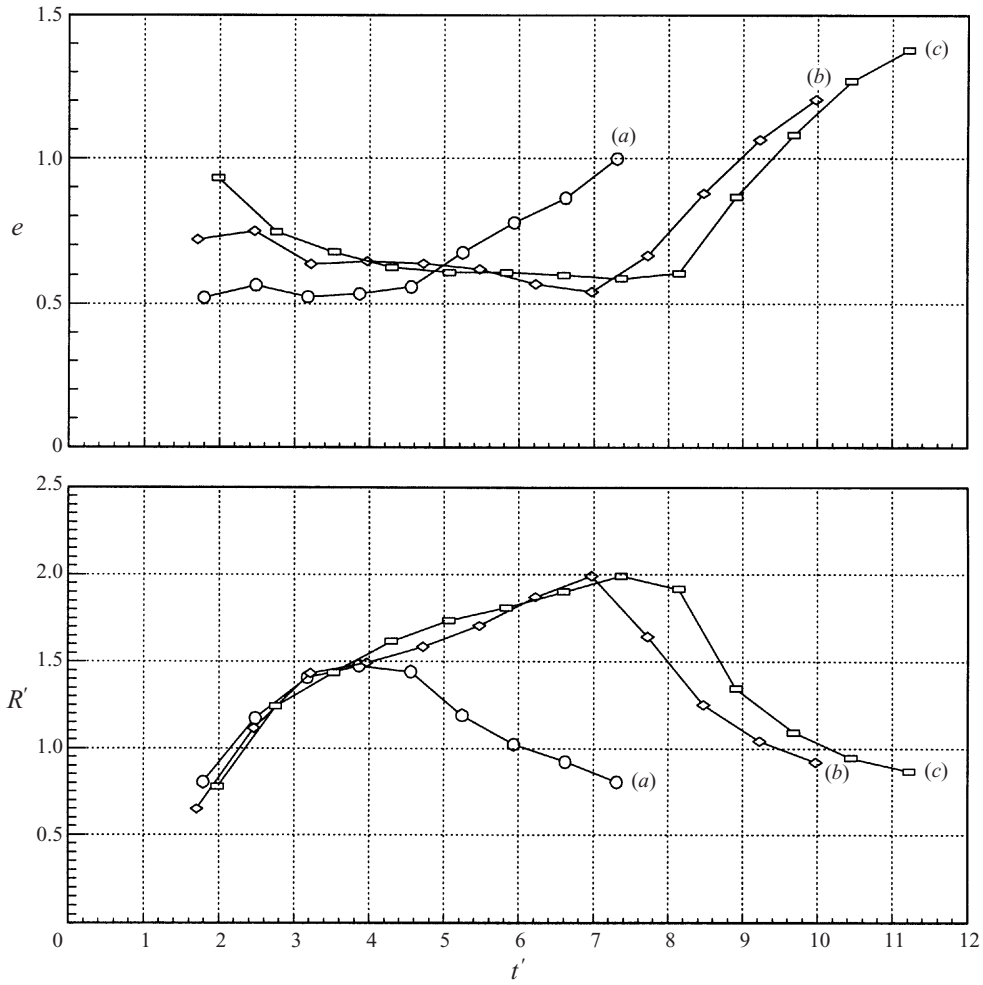


FIGURE 3. The e ratio, defined as the cavity width divided by twice the cavity depth, and dimensionless cavity depth (R') against dimensionless time (t') for the coalescing drops. (a) $Fr = 90$, $We = 43$, $d = 1.86\,\mathrm{mm}$ and $u = 1.29\,\mathrm{m\,s^{-1}}$ for the drop sequence in figure 2(a). (b) $Fr = 119$, $We = 70$, $d = 2.07\,\mathrm{mm}$ and $u = 1.56\,\mathrm{m\,s^{-1}}$ for the drop sequence in figure 2(b). (c) $Fr = 126$, $We = 75$, $d = 2.09\,\mathrm{mm}$ and $u = 1.61\,\mathrm{m\,s^{-1}}$.

3.2. *Bubble entrapment and thin high-speed jets*

Figure 2(c), for the case of $Fr = 146$ and $We = 87$, shows the formation of a thin high-speed jet. The base of the cavity grows smoothly till about 7 ms after impact ($t' = 6$ in figure 3). During that time, a sharp corner initially at the equatorial position of the cavity moves down along the cavity wall. After 7 ms, the sharp corner grows inwards with an ever steepening capillary wave. Compared to figure 2(b), a much sharper tip is formed at 12 ms after impact and this tip rebounds resulting in the formation of a thin high-speed jet, defined as the narrow jet formed from the centre of the cavity. It breaks into small droplets before rising above the wave swell and becoming visible. The thin high-speed jet does not rise significantly above the top of the wave swell.

https://doi.org/10.1017/S0022112000002500 Published online by Cambridge University Press

We	*Fr*	Bubble diameter (mm)	Jet droplet diameters and velocities ($m\,s^{-1}$)
81	133		0.17 (4.8), 0.17 (2.2), 0.19 (1.2)
87	146	0.08	0.11 (10.5), 0.09 (5.0), 0.14 (3.8), 0.11 (3.40)
			0.07 (2.8), 0.11 (2.6), 0.20 (1.3), 0.23 (0.9)
92	152		0.10 (5.6), 0.09 (3.9), 0.10 (2.7), 0.12 (2.2)
			0.27 (0.8), 0.54 (0.1)
97	160	0.31	0.11 (4.3), 0.08 (3.0), 0.12 (2.4), 0.54 (0.3)
104	174	0.54	0.10 (4.9), 0.09 (4.9), 0.13 (3.0), 0.24 (1.1)
			0.42 (0.4)
107	178	0.62	0.13 (2.8), 0.26 (1.4), 0.26 (0.8)
134	219	0.78	0.14 (7.4), 0.14 (4.8), 0.14 (3.6), 0.2 (2.5)
			0.13 (2.3), 0.3 (1.1)
161	186	0.79	0.15 (4.6), 0.18 (2.1), 0.24 (1.2)
186	301	0.76, 0.34	0.13 (5.0), 0.13 (3.3), 0.34 (1.7)
209	341	0.86, 0.26	0.32 (2.2)
234	379		0.31 (3.0), 0.24 (2.5), 1.70 (0.0)
216	449		0.13 (4.3), 0.17 (3.5), 0.31 (0.8)

TABLE 1. Entrapped bubble diameters, droplet diameters and velocities (shown in brackets) for the high-speed Rayleigh jet regime measured from photographs. The velocity is measured from the first two frames where the droplet first appears. The diameter and velocities are those of the splash drops that form from the jet break-up and relate to a single experiment, not several measurements.

Table 1 lists the jet droplet diameters and initial velocities measured. The velocities of the droplets that break off from the high-speed jet attain up to 10.5 (± 0.03) $m\,s^{-1}$. Rein (1996) showed that the lower limit in the (We, Fr)-plane (figure 1) for the formation of a thin high-speed jet coincides with the formation of an entrained bubble. In this set of experiments, the start of the high-speed jet occurs in a region significantly below the theoretical curve of OP(I) and in the region where Rein claims that only coalescence occurs with a thick jet forming. Figure 3 of Rein's (1996) paper shows a thick jet rising much higher than seen in the current photographs of the coalescence regime: the thick jet of Rein's figure 3 is similar to the jet seen 19 ms after impact in figure 2(c). Similar results for the lower limit were obtained for the 16G needle drops (see figure 1). The transition from the coalescence-only regime to the thin high-speed jet regime is quite sudden, much more so than suggested by Rein (1996).

Once the bubble entrapment regime was reached, bubble entrapment occurred over a fairly large range of *We* and *Fr* as seen in figures 2(c), 2(d) and 2(e) and table 1. The digitized film had a resolution of 30 μm allowing drops and bubbles to be detected down to 30 μm, but only drops and bubbles larger than 60 μm can be measured reliably. The pictures also showed that sharp tips were formed at the cavity base in the jetting regime below and above the bubble entrapment regime. The entrained bubble diameter rises rapidly from 0.1 mm as the *We* and *Fr* values increase to a constant diameter of around 0.6 to 0.8 mm for most of the conditions in the bubble entrapment regime. In the regime for the 16G needle drops, bubble entrapment was dependent on the shape of the drop at impact. Prolate drops did not entrap bubbles. Oblate drops and drops with shapes intermediate between prolate and oblate resulted in bubble entrapment. The drop shape parameter was not investigated in detail as the 16G results were only used to delineate the lower and upper limits of the bubble entrapment regime.

https://doi.org/10.1017/S0022112000002500 Published online by Cambridge University Press

To ascertain whether smaller entrapped bubbles were missed in the thin high-speed jet regime, the apparatus was re-assembled and a series of runs carried out with a variation of 2 mm in the drop height for the 33G needle. This resulted in Fr being varied by 2 and We by 1 between different runs. The runs were repeated, but not consecutively, up to three times at selected heights and this showed that the results were repeatable even with such a small variation in drop height. In this second run, the resolution was taken down to 10 μm and confirmed that no bubbles were entrapped even though the thin high-speed jet was consistently observed.

However, it was found that within the region where only thin high-speed jets formed, there were certain values of We and Fr that did not produce a jet (unfilled diamonds in figure 1). Instead, a thicker jet similar to Rein's figure 3 was observed. This was confirmed with repeated runs. Image analysis showed that the drop was at its maximum oblate shape at impact. The dimensionless number window for this to occur was approximately 1 for We and 2 for Fr. However, above $Fr = 140$, the shape of the drop did not matter and thin high-speed jets were obtained until the bubble entrapment regime was reached. The region where bubble entrapment began was studied with video equipped with a close-up lens that resolved up to 10 μm. The entrapped bubble sizes captured from a large number of observation varied from 100 to 250 μm, the size increase occurring over a change in Fr of about 10. Smaller entrapped bubble sizes were not observed.

3.2.1. *An explanation for the thin high-speed jets*

It is well established that bubble entrapment results in the formation of a high-pressure stagnation point where the cavity closes. This high pressure results in the formation of a high-speed jet. Table 1 shows that the appearance of bubble entrapment is fairly abrupt with a finite bubble size produced. This experimental observation is consistent with Pumphrey & Elmore's (1990) and OP(I) observation that the entrapped bubble has a narrow size range over a wide range of impact velocities.

An explanation for this high-speed jet can be based on an earlier description by Longuet-Higgins (1990) in relation to sound production by raindrops. After impact, the cavity is stretched in the equatorial direction. A sharp corner arises where the cavity and wave swell meet. It was noted in the experiments that when the sharp corner was observed, it always appeared after the wave swell had reached its maximum amplitude. The movement of this sharp corner tracks a capillary wave as it propagates downwards to the polar end or base of the cavity. While the capillary wave is propagating, the cavity base stops growing and the cavity starts collapsing. During cavity collapse, the capillary wave is being focused into the cavity base. As the capillary wave is focused, it grows in aspect ratio and becomes steeper. The steepening causes the cavity base to grow downwards again to form a sharp point. The sharp point retracts and when the retraction is rapid enough, a high-speed jet is formed. With increasing impact speeds, the point is sharper, resulting in a faster retraction and hence a faster thin high-speed jet. This is in agreement with the experiments where the splash drop velocities are higher for $Fr = 146$ and $We = 87$ than for $Fr = 133$ and $We = 81$. When the impact speed increases, the cavity takes longer to begin collapsing. This allows the capillary wave to progress to a steeper wave and it meets and entraps a bubble before the sharp point can retract.

The nonlinear effects of progressive capillary waves have been studied (Crapper 1957; Longuet-Higgins 1988) and the wave crests show a rounding effect similar to that seen in figures 2(*b*) and 2(*c*). Although the capillary wave in this case is

https://doi.org/10.1017/S0022112000002500 Published online by Cambridge University Press

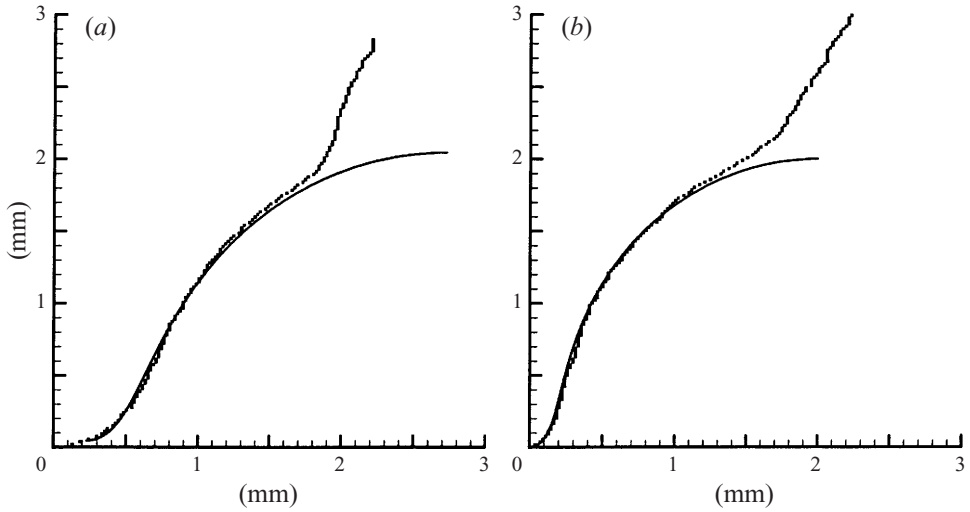


FIGURE 4. Pixel outline of the cavity at the last frame before collapse compared to the Crapper wave profile. (*a*) $Fr = 121$, $We = 68.7$, $d = 2.04$ mm, and $u = 1.56\,\mathrm{m\,s^{-1}}$. $a/\lambda = 0.4$ for the Crapper wave. The Crapper wave was shifted 0.25 mm to the right to match the cavity shape. (*b*) $Fr = 123$, $We = 69.7$, $d = 2.04$ mm, and $u = 1.57\,\mathrm{m\,s^{-1}}$. $a/\lambda = 0.5$ for the Crapper wave.

axisymmetric and converging towards the centre, a rough comparison of the wave profile can be made with the shapes given by Crapper (1957). Figure 4 shows the comparison for two cases, just before and just after the start of the high-speed jet regime. It is found possible to match the curves for different a/λ values (a is the wave amplitude and λ is the wavelength as defined by Crapper) to the experimental cavity shapes. The a/λ values increase on going from no jet to a high-speed thin jet. The fit has been obtained by assuming that $a = 2$ mm, which is about the size of the drop diameter. Since the Crapper wave encloses a bubble in its trough when $a/\lambda = 0.73$, bubble entrapment will begin with a bubble of finite size. Taking $a = 2$ mm, the entrapped bubble diameter is around 0.1 mm which is consistent with experimental observations. With bubble entrapment, the capillary wave collapses with a substantial protrusion that meets to entrap the bubble. The shape is not rounded, so no fits were possible with any value of the Crapper wave.

The speed of this converging wave was obtained by measuring the speed of the converging front at the flat base of the cavity (e.g. frames at 5–8 ms in figure 2*b*). Values of 0.43 to $0.5\,\mathrm{m\,s^{-1}}$ were obtained. This is approximately within the range of capillary wave speed for a wavelength about equal to the drop diameter. It was found that the velocity of the capillary wave increased by up to 20% while it was converging towards the cavity centerline but there were not enough image frames to get an accurate estimate of velocity variations. This indicated that the wavelength was decreasing while it converged. This is consistent with the fits for figure 4 that required a to be kept constant while a/λ was increased.

The experimental results suggest that once the capillary wave passes a given a/λ value, it is possible for the wave trough to retract rapidly and form a high-speed jet when the capillary forces in the trough can overcome the force of the wave converging to form the trough. An approximate value of 0.5 is obtained from the experimental results. In many physical situations, a critical vertex angle of 109.5° exists where a high-speed jet is formed (Longuet-Higgins 1990). Its applicability to this case is

https://doi.org/10.1017/S0022112000002500 Published online by Cambridge University Press

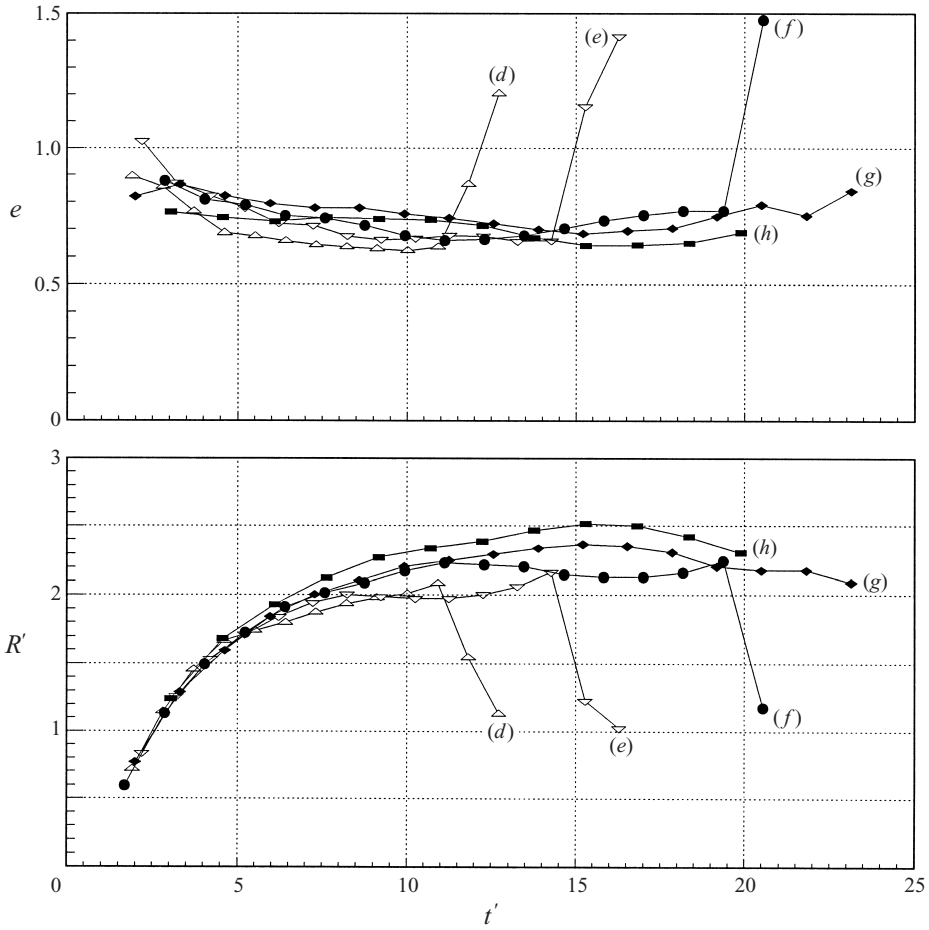


FIGURE 5. The e ratio and dimensionless cavity depth (R') against dimensionless time (t') for the high-speed jet regime. (d) $Fr = 174$, $We = 104$, $d = 2.10\,\text{mm}$ and $u = 1.89\,\text{m s}^{-1}$. ($e$) $Fr = 219$, $We = 134$, $d = 2.12\,\text{mm}$ and $u = 2.13\,\text{m s}^{-1}$ for the drop sequence in figure 2(d). (f) $Fr = 301$, $We = 186$, $d = 2.13\,\text{mm}$ and $u = 2.51\,\text{m s}^{-1}$ for the drop sequence in figure 2(e). (g) $Fr = 379$, $We = 234$, $d = 2.13\,\text{mm}$ and $u = 2.81\,\text{m s}^{-1}$. ($h$) $Fr = 449$, $We = 216$, $d = 1.88\,\text{mm}$ and $u = 2.88\,\text{m s}^{-1}$ for the drop sequence in figure 2(f).

slightly different as a gas cavity retracts and forms a high-speed jet. For the Crapper wave, when $a/\lambda > 0.31$ there is a slope forming a vertex angle of 109.5° or less. In § 3.2.3, the cavity was found not to reach the critical angle when only a high-speed jet occurred. However, the images obtained suggest that the sharp tip steepens quite independently of the rest of the cavity. Another possibility for the condition for the high-speed jet to form could be when there is a vertical slope of the Crapper wave profile (i.e. $a/\lambda > 0.64$), but a more accurate resolution of the exact value of a/λ is not possible with the experimental setup as the final stages occur too rapidly.

As the capillary wave speed is proportional to the square root of the surface tension, a decrease in the surface tension by a surfactant will result in a slower capillary wave and hence a shift to a higher *We*. This may result in a move out of the jet formation and bubble entrapment regime. This effect is observed in figure 23 of Pumphrey & Elmore (1990).

https://doi.org/10.1017/S0022112000002500 Published online by Cambridge University Press

3.2.2. *Cavity dynamics*

In the bubble entrapment regime, the cavity is initially oblate in shape. Figure 5 shows that a plot of the dimensionless cavity depth versus dimensionless time collapses to a single line at the early stages of cavity formation. The cavity grows continuously in a U-shape (figure 2*c–f*). Just before collapse the sides near the base contract sharply to form a V-shaped cavity.

As the cavity expands the wave swell amplitude stops increasing and continues travelling outwards. As noted earlier, this coincides with the appearance of the sharp corner which starts travelling down the cavity. The experimental setup does not provide clear evidence of whether this sharp corner is a direct result of the collapse of the wave swell. The moving sharp corner causes a steepening of the sides of the cavity. Initially, the moving sharp corner retards the outward growth of the cavity while the downward growth is unaffected. The decrease in the e ratio with time is halted and it approaches a constant value as the cavity continues to grow. The cavity stops growing downwards and reverses direction when the sharp corner is part of the way down the cavity wall ($t' = 8$–12 for curve (e), $t' = 11$–16 for curve (f) in figure 5). But this reverse motion is arrested by the sharp corner forming a steep capillary wave that converges towards the base of the cavity, which expands again ($t' = 13$–14 for curve (e), $t' = 17$–19 for curve (f) in figure 5) as the capillary wave steepens. While the cavity base is expanding for the second time, other parts of the cavity above the base continue collapsing. The capillary wave meets at a point just above the cavity base leading to bubble pinch off. The bubble formed is accelerated downwards. The photographs show that the motion of the sharp corner causes the cavity sides to collapse at different times. This explanation is consistent with the findings of Morton *et al.* (2000). OP(I) noted that their pictures showed that the sidewalls move in with a velocity that increases with depth. In contrast, superposing the cavity outlines from successive time frames (figure 2*c*, *d*) shows that the moving sharp corner increases the cavity width and the collapse of the sidewalls near the cavity base starts some time after the cavity base has started retracting.

The sharp corner that travels down the cavity forms sharper edges as *We* and *Fr* increase. This leads to the cavity taking a polygonal shape initially with seven or eight faces which reduces to an inverted triangle just before bubble entrapment. The high-speed jet regimes without bubble entrapment are marked by the presence of a sharp tip just before jet formation (12 ms in figure 2(*c*) and 16 ms in figure 2(*f*)) indicating that the capillary wave is not steep enough to entrap a bubble.

3.2.3. *Cone angle*

In an analytic model of sound production by raindrops based on potential flow theory, Longuet-Higgins (1990) presented a criterion for the production of a bubble from an exact solution for conical flow. The time dependence was found to develop a singularity at the instant when the vertex angle of the conical boundary passes through the critical angle of 109.5° and a bubble will be entrained. Direct measurement of the cone angle at the base of the cavity prior to the formation of the high-speed jet to confirm the critical angle of 109.5° was not possible as the cone angle varied too rapidly to be fully captured by the drum camera. Longuet-Higgins also showed that the time dependence of the cone angle (2γ) is given by

$$\tan\gamma \approx \sqrt{2}(1 - \tfrac{3}{2}\tau^{2/3}), \tag{3.1}$$

https://doi.org/10.1017/S0022112000002500 Published online by Cambridge University Press

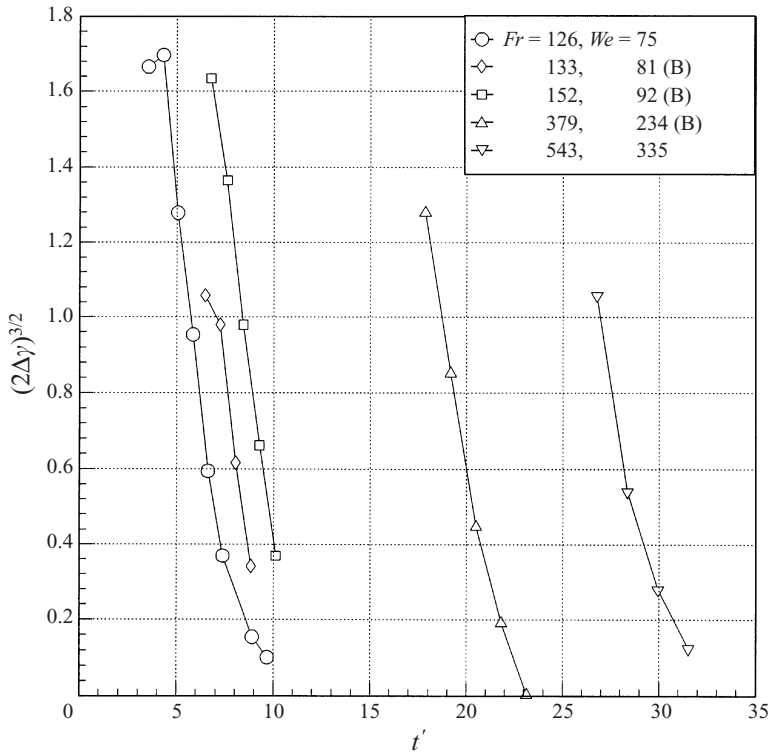


FIGURE 6. Variation of the cone angle departure from its limiting value with dimensionless time for the collapsing cavity. B in the legend denotes bubble entrapment cases.

where τ is linearly related to the dimensionless time. The departure of the cone angle from its limiting value is

$$\Delta\gamma = \arctan\sqrt{2} - \gamma. \tag{3.2}$$

Plotting $(2\Delta\gamma)^{3/2}$ against dimensionless time should give a straight line if the results satisfy equation (3.1) and provide an indirect test of the theory. Longuet-Higgins has only shown that this scaling applies for the numerical simulations of OP(I). Measurement of the experimental cone angle is difficult as the cavity surface is not smooth and a well defined cone allowing precise measurements is generally not observed. Nevertheless, figure 6 shows that equation (3.1) is satisfied for the cases where bubble entrapment occurs. The extrapolation of the line gives an approximate dimensionless time for the appearance of the high-speed jet. For the cases where there is no bubble entrapment, the line curves away as the critical angle is approached. It can be concluded that the simple analytical model of Longuet-Higgins holds for bubble entrapment. For the case of $Fr = 126$ and $We = 75$, a thin high-speed jet is formed but the line curves away as the critical angle is approached. The vertex angle of the capillary wave trough varied too quickly to provide adequate points for verifying whether the trough itself satisfied this critical angle criterion. However, the vertex cone angle of the sharp point measured between 35° and 40° for the frame just before the jet forms. In the coalescence regime, the cone decreased to about 50° before expanding again during collapse.

https://doi.org/10.1017/S0022112000002500 Published online by Cambridge University Press

3.3. *The upper limit to bubble entrapment*

The upper limit for bubble entrapment is close to OP(I)'s theoretical curve. However, the formation of the high-speed jet persist to higher *Fr* and *We*, resulting in a larger regime for high-speed jet formation. Figure 2(*f*) shows that the capillary wave meets to form a sharp point at the cavity base (16 ms). Photographs of a number of sharp points showed that the points were not axisymmetric, in contrast to those formed in the lower regime of the high-speed jets. A second set of more closely spaced runs was carried out and the formation of the high-speed jet for the 33G needle drops was found to persist till around $Fr = 425$–446 and $We = 244$–251 which is above the upper limit of OP(I)'s theoretical curves for bubble entrapment. The results for the 16G needle drops exhibit similar behaviour. The results shows that the regime for bubble entrapment is a subset of the high-speed jet regime. In the bubble entrapment regime, there are at least six to ten drops of varying sizes ejected from the jet with the first drop appearing above the wave swell before the jet appears. The velocities of the first few small drops are always greater than the impacting drop velocity. Once the high-speed jet regime boundary is crossed, the jet breaks up with two or fewer large drops after the jet has grown significantly above the wave swell. These larger splash drops have velocities less than that of the impacting drop velocity.

3.4. *Formation of the crown*

The wave swell was earlier defined as the rim of the impact cavity that is initially intact and subsequently spreads radially outwards. The crown is defined here as the portion of the rim that breaks up ejecting small splash droplets.

The smooth wave front that moves up the impacting drop faster than the drop moves into the target liquid was found to separate from the drop while it was still entering the bulk liquid. The wave formed an annular spray, which can also be seen more clearly in a downwards view on page 42 of Worthington's (1908) book. The appearance of the annular spray coincides with the upper limit for bubble entrapment. Figure 7 shows the behaviour for three different *Fr* and *We* covering below, at, and above the transition for spray formation. Figure 7(*b*) shows the annular spray forming which ejects fine drops horizontally but does not form a fully developed crown until at a later time. In figure 7(*c*) a fully formed crown is shown with larger splash drops ejected at an angle about 45° to the horizontal. The time taken from the formation of the spray to the breakup of the largest drop from the crown is about 0.5 ms. This is extremely rapid and is only partially captured by the camera. The photographs show that spray formation marks the start of crown breakup. As *Fr* and *We* increase, the crown breakup becomes more and more distinct until a distinct annular crown is formed as in figure 7(*c*).

It is possible to piece the event together from different drop experiments. On impact, a smooth wave front of the target fluid moves up the impacting drop. When the smooth wave front is able to overcome the surface tension forces holding it to the drop surface, a spray is formed and breaks up before the drop has completely entered the bulk liquid. The drop continues to spread on the surface of the cavity, while the rest of the wave front that has not broken up in a spray then thickens to form the wave swell at the rim of the cavity. Numerical simulations by Morton *et al.* (2000) show that the drop fluid for this thick jet regime spreads evenly over the surface of the cavity and continues to be propagated out radially with the wave swell. At higher *Fr* and *We*, there is more energy than can be dissipated by the spray and a crown develops that ejects larger drops. After the larger drops have been ejected, the wave swell that remains continues to propagate outwards. When a crown is formed,

https://doi.org/10.1017/S0022112000002500 Published online by Cambridge University Press

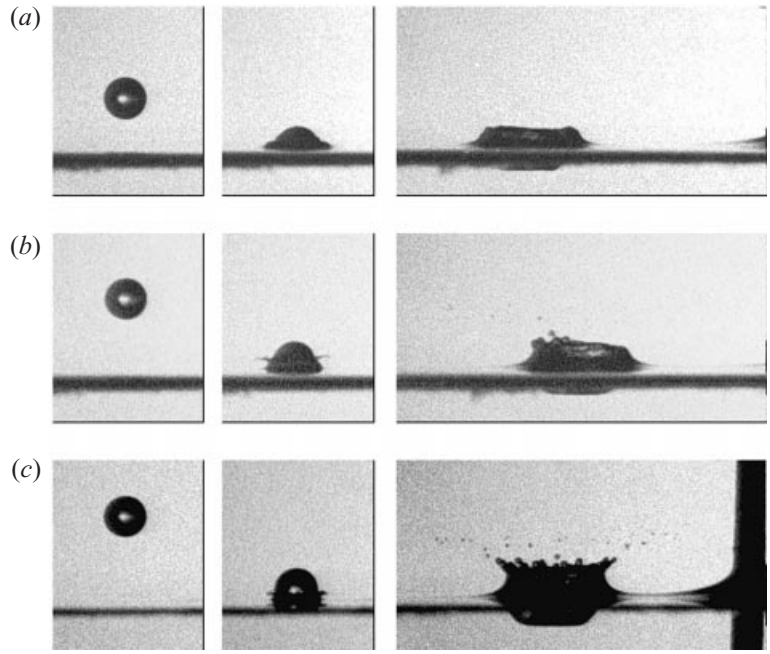


FIGURE 7. Three consecutive frames separated by 1 ms for three different conditions showing the phenomena associated with the transition to crown formation: (*a*) $Fr = 301$, $We = 186$, $d = 2.13$ mm and $u = 2.51\,\mathrm{m\,s^{-1}}$; (*b*) $Fr = 490$, $We = 296$, $d = 2.11$ mm and $u = 3.18\,\mathrm{m\,s^{-1}}$ – a spray can be seen and fine drops indicating a small crown; (*c*) $Fr = 639$, $We = 395$, $d = 2.13$ mm and $u = 3.65\,\mathrm{m\,s^{-1}}$ – a spray is visible and the crown is well formed (The dark outline to the right in the last photograph is the outline of the thin stem joining the marker plates and does not affect the experiment.)

the cavity rim is disturbed with numerous capillary waves being visible on its surface. These waves do not dissipate as quickly as in the previous cases with lower Fr and We for the bubble entrapment regime where they dissipate before cavity collapse occurs. The waves dissipate quite late during the cavity collapse stage and their influence on the cavity collapse is discussed in the next section.

3.5. *Thick jet regime*

The cavity behaviour in the thick jet regime is shown in figure 2*g*, *h*. The transition from the high-speed jet to the thick jet occurs within a We range of 5 and Fr range of 20.

There are a number of differences in cavity behaviour between this thick jet regime and the high-speed jet regime. First, the drop forms a spray during impact. Second, an unstable rim is formed which subsequently results in a crown. Experimentally, the appearance of the spray and crown coincides with the disappearance of the thin high-speed jet. Third, the surface of the wave swell is much more disturbed with numerous small surface waves being present in the cavity which take longer to damp out after drop impact (at 17 ms (dimensionless time of 25) for $Fr = 454$ and $We = 283$ compared with at 8 ms (dimensionless time of 12) for $Fr = 449$ and $We = 216$). Fourth, the wave front travelling down the cavity appears much later and the intermediate polygonal shapes are more pronounced. The vertices of the polygon can be seen travelling downwards. Photograph of the cavity surface in Worthington (1908) show that the cavity surface is covered with many capillary waves. Fifth, the base of the cavity during collapse is not flat but is covered with smaller capillary

https://doi.org/10.1017/S0022112000002500 Published online by Cambridge University Press

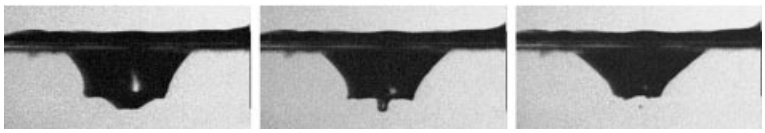


FIGURE 8. Formation of a secondary bubble for the case $Fr = 639$, $We = 395$, $d = 2.13$ mm and $u = 3.65\,\mathrm{m\,s^{-1}}$. Note the wavy surface of the cavity base in contrast to the smooth cavity base for the cases in the bubble entrapment regime. Consecutive frames are separated by 1 ms.

We	*Fr*	Splash drop diameter (mm)	Velocity of splash drop ($\mathrm{m\,s^{-1}}$)	Angle (deg.)	Jet height (mm)
251	445	0.93, 1.39	1.36, 0.43	33, 73	3.96, 6.93
283	454	1.52	0.71	31	5.99
296	490	1.91	0.51	34	7.11
323	519	2.05	0.45	34	7.77
335	543	2.31	0.30	31	8.63
344	577	2.30	0.38	32	8.76
394	639	2.31	0.39	32	9.75
351	711	2.21	0.41	32	7.89

TABLE 2. Size and velocity of splash drop pinched off in the thick jet regime, angle subtended by the jet at the point just below the detaching splash drop and height reached by the jet when breakup occurs.

waves which give rise to the secondary entrapment of bubbles. Figure 8 shows an entrained bubble formed for the $Fr = 639$ and $We = 395$ case.

Sixth, a thick jet is formed with splash drops pinching off that are comparable in size to the impacting drop. Near the transition from the thin high-speed jet to the thick jet regime, the jet initially breaks up to form two splash drops but rapidly settles down with increasing *Fr* and *We* to give only one large splash drop comparable in diameter to the impacting drop. The splash drop sizes and velocities are given in table 2. The velocity of the splash drop measured between two successive frames just after detachment shows that the splash drop velocity falls as *Fr* increases. The height of the jet measured in the frame prior to the detachment of the splash drop, in general, increases with *Fr*. However, at higher *Fr*, the crown closes back on itself forming a barrier to the thick jet (Engel 1966) and limits the height that the thick jet can reach. The angle subtended by the thick jet just below the first detaching splash drop measured prior to detachment is fairly consistent and between 31° and 34°.

The cavity formed is more hemispherical than in the regimes discussed so far, as shown in figure 9 but the assumption that the expansion of the cavity is fully hemispherical in the thick jet regime was not confirmed experimentally. Figure 9 shows that for cases (*g*) and (*h*) in this regime, the *e* ratio over most of the cavity lifetime is about 0.75. Figures 2(*g*) and 2(*h*) show that the inward travelling wave appears later and the expanding tip of the cavity base has reversed its motion and contracted long before the wave reaches it. The upward rising cavity base meets the inward travelling wave and thereafter the flat cavity bottom with numerous capillary waves appears. Figure 9 shows that the cavity depth remains unchanged for ten or more dimensionless times, after which the cavity base collapses to form a thick jet.

https://doi.org/10.1017/S0022112000002500 Published online by Cambridge University Press

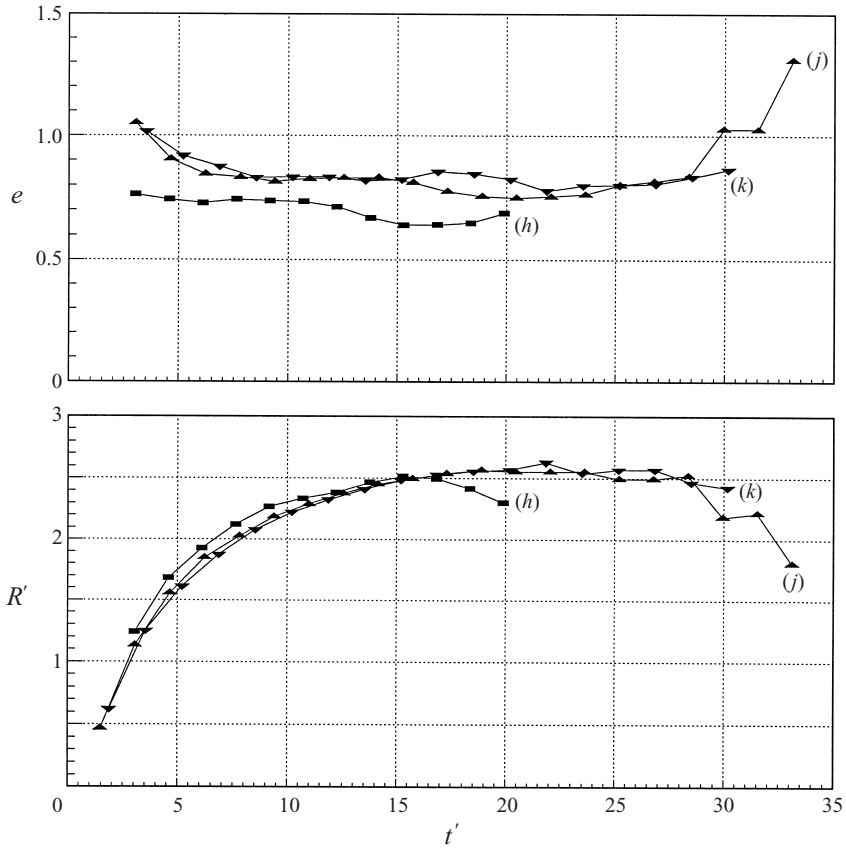


FIGURE 9. The e ratio and dimensionless cavity depth (R') for the thick jet regime. (h) $Fr = 449$, $We = 216$, $d = 1.88$ mm and $u = 2.88\,\mathrm{m\,s^{-1}}$ for the drop sequence in figure 2(f). (j) $Fr = 543$, $We = 335$, $d = 2.13$ mm and $u = 3.37\,\mathrm{m\,s^{-1}}$ for the drop sequence in figure 2(h). (k) $Fr = 600$, $We = 368$, $d = 2.12$ mm and $u = 3.53\,\mathrm{m\,s^{-1}}$.

3.6. *Maximum cavity depth*

Following Pumphrey & Elmore (1990) and relating the drop kinetic energy to the potential energy of the mass displaced for a hemispherical cavity gives

$$R'_m = \left(\frac{Fr}{3\rho'}\right)^{1/4} \tag{3.3}$$

where $R'_m = R_{max}/d$, R_{max} is the maximum cavity depth, d is the drop diameter, ρ' is the density ratio $\rho_{target}/\rho_{impactor}$ or ρ_t/ρ_i. In figure 10 R'_m against Fr is plotted for a large number of water drop experiments, both from the literature and from the current set of experiments. As Pumphrey & Elmore's (1990) paper only reported the value of $d^{3/4}u^{1/2}$, it is not possible to include their results. The theoretical line overpredicts the maximum cavity diameter because the energy of the surfaces formed and the wave swell has not been taken into account and increases with increasing Fr. In dimensional units, plotting R_{max} against $d^{3/4}u^{1/2}$, we find that Pumphrey & Elmore's (1990) cavity sizes are significantly larger than in this study or any other published results except that of Cai (1989*a*). However, a fuller description of Cai's (1989*b*) experimental procedure places serious doubts on the accuracy of those results as the

https://doi.org/10.1017/S0022112000002500 Published online by Cambridge University Press

target liquid in the trough was moving with a constant velocity and the dropper was driven continuously by a motor to different heights simultaneously. In Pumphrey & Elmore's (1990) case, a third of the results were on or above the theoretical line, which indicated that the cavity's potential energy was either equal to or larger than that supplied by the drop kinetic energy, and this occurred for higher values of $d^{3/4}u^{1/2}$ where impacting drop surface tension energy is small compared to the impacting drop kinetic energy. Figure 10 does show that the $Fr^{1/4}$ scaling applies to the data presented and a least-squares fit gives

$$R'_m = 0.727 \left(\frac{Fr}{3\rho'}\right)^{1/4}. \tag{3.4}$$

Equation (3.4) shows that only 28% of the impacting drop kinetic energy is converted to the cavity potential energy. At low Froude numbers, the effect of surface tension becomes important as the maximum cavity size diminishes rapidly with decreasing Froude number. A correction to equation (3.3) has been given by Prosperetti & Oğuz (1993). Since equation 3.3 assumes a hemispherical cavity shape which is strictly valid for high-momentum drops, the data of Fink, Gault & Greeley (1984) for hypervelocity impacts of solid spheres in water and silicon oil were used to find the range of validity of equation (3.3) (see figure 10). The hypervelocity data also show the same $(Fr/\rho')^{1/4}$ dependence given by equation (3.3) but the points are shifted to the right. Since the formation of a crown and loss of material occur while the cavity is forming for high Fr, it is expected that there would be a smaller R'_m for a given Fr. Nevertheless, equation (3.4) is near the low-viscosity results of Fink *et al.* (1984) indicating the scaling is valid to high Fr. The high-viscosity results show significantly smaller maximum cavity sizes over the same Fr range.

3.7. *Time to reach maximum cavity depth*

The scaling for the growth of the cavity with time can be estimated from a balance between the kinetic energy of the fluid and the drop kinetic energy based on an approach similar to Engel (1967) but assuming that the drop impact represents a source. The potential of the fluid around the cavity be then be approximated by

$$\phi = \frac{A}{r}. \tag{3.5}$$

The radial velocity is

$$v_r = -\frac{\partial \phi}{\partial r} = \frac{A}{r^2}, \tag{3.6}$$

and the tangential velocity is 0. The resultant velocity, $q = (v_r^2 + v_\theta^2)^{1/2}$ is then given by A/r^2. At the cavity wall, where $r = R$, the resultant velocity is equal to $\mathrm{d}R/\mathrm{d}t$, that is

$$\frac{\mathrm{d}R}{\mathrm{d}t} = \frac{A}{R^2}. \tag{3.7}$$

Solving for A gives

$$\phi = \frac{R^2}{r}\frac{\mathrm{d}R}{\mathrm{d}t}. \tag{3.8}$$

The kinetic energy in the target liquid below the original surface of the liquid for the cavity at a position of R and resultant velocity of $\mathrm{d}R/\mathrm{d}t$ is given by

$$E_k = -(\rho/2)\iint \phi \frac{\partial \phi}{\partial r}\mathrm{d}S, \tag{3.9}$$

https://doi.org/10.1017/S0022112000002500 Published online by Cambridge University Press

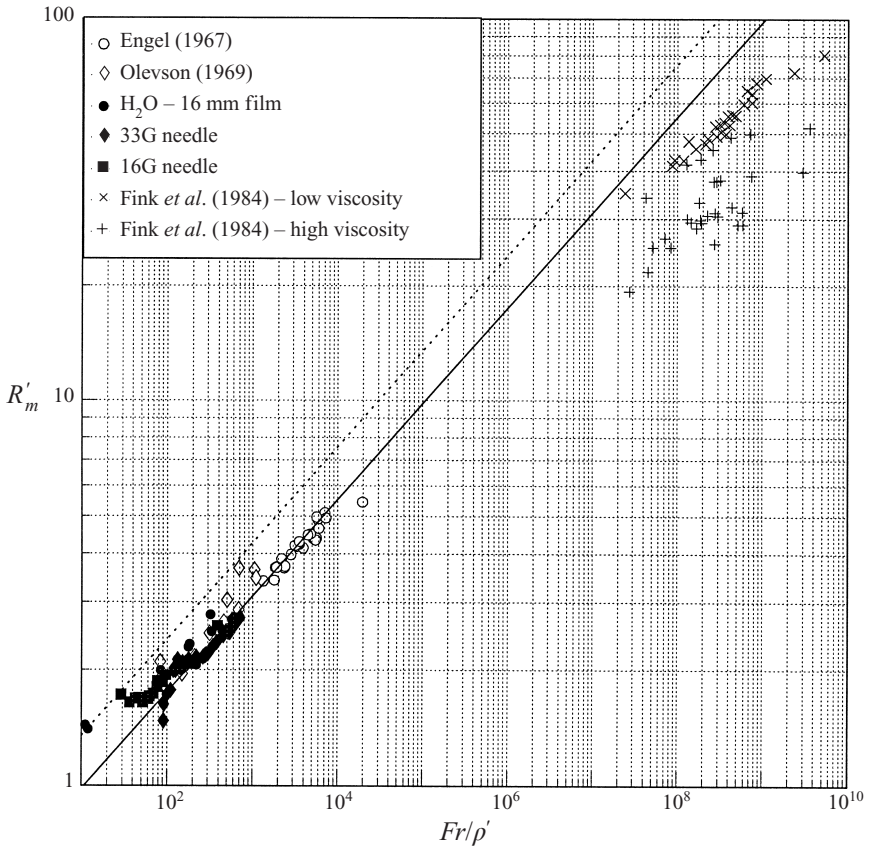


FIGURE 10. Variation of the dimensionless maximum cavity depth with the Froude number for data from this study and the literature. The dotted line is the theoretical prediction, and the solid line is the least-squares fit for water–water impacts. The hypervelocity data of Fink *et al.* (1984) for solid spheres into liquids is included. The density differences between the solid projectiles and liquid target have been taken into account in the Fr/ρ' term. The low-viscosity data are for water and silicon oil of viscosities of 200 and 2850 cP. The high-viscosity data are for silicon oil of viscosities of 25 600 and 60 000 cP.

where S is a surface element. Substituting for ϕ and $\partial\phi/\partial r$ gives

$$\begin{aligned} E_k &= -\frac{\rho}{2}\iint \frac{R^4}{r^3}\left(\frac{\mathrm{d}R}{\mathrm{d}t}\right)^2 \mathrm{d}S, \\ &= \pi\rho R^3\left(\frac{\mathrm{d}R}{\mathrm{d}t}\right)^2 \int_0^{\pi/2} \sin\theta \mathrm{d}\theta, \\ &= \pi\rho R^3\left(\frac{\mathrm{d}R}{\mathrm{d}t}\right)^2. \end{aligned} \tag{3.10}$$

If Fr is large, then the kinetic energy of the mean flow driven by the expanding cavity does not change substantially during the early stages of cavity formation. For a constant kinetic energy, equation (3.10) gives the result that $t \propto R^{5/2}$ (a referee kindly pointed out that this had been derived earlier by Birkhoff (1954) in relation to collapsing spherical cavities who also showed that the expansion phase is stable but the collapse phase is unstable). A plot of the dimensionless cavity depth against

https://doi.org/10.1017/S0022112000002500 Published online by Cambridge University Press

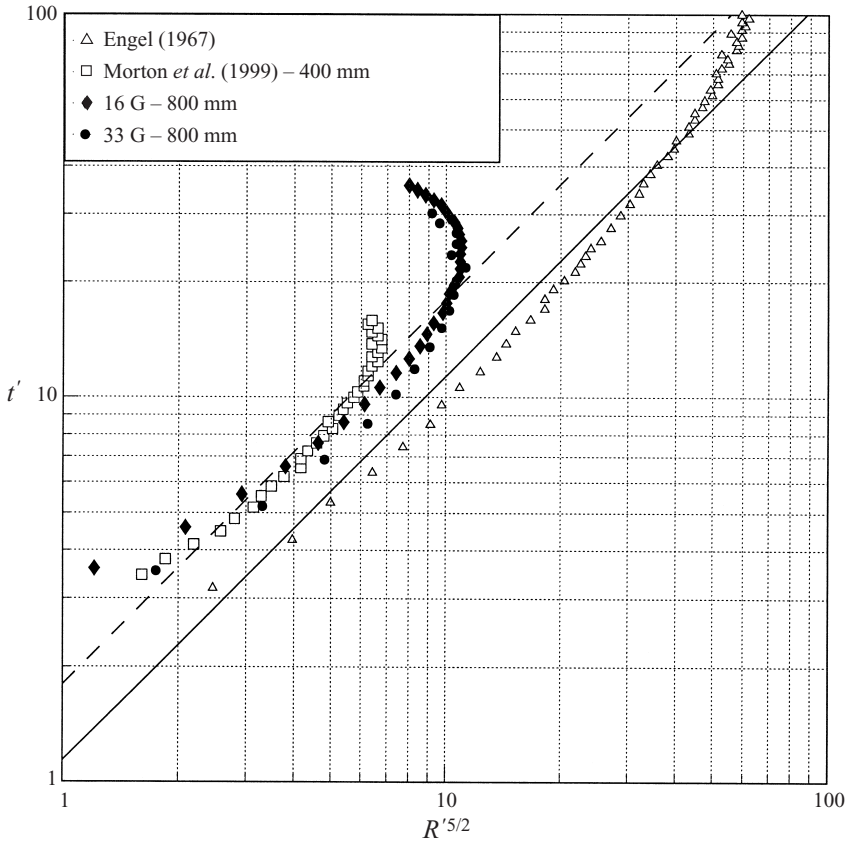


FIGURE 11. Variation of the cavity depth with time for water drops impacting onto water. Engel's (1967) data are for $Fr = 6950$, $We = 19360$, $d = 4.55\,\text{mm}$ and $u = 17.61\,\text{m s}^{-1}$ at 3644 frames per second with the least-squares-fit solid line of $t' = 1.14R'^{5/2}$; Morton *et al.* (2000) is for $Fr = 220$, $We = 248$, $d = 2.90\,\text{mm}$ and $u = 2.50\,\text{m s}^{-1}$ at 2500 frames per second with the least-squares-fit dashed line of $t' = 1.80R'^{5/2}$; the 16G and 33G from this study are for a fall height of 800 mm with $Fr = 387$, $We = 756$, $d = 3.77\,\text{mm}$ and $u = 3.78\,\text{m s}^{-1}$ and $Fr = 600$, $We = 368$, $d = 2.12\,\text{mm}$ and $u = 3.53\,\text{m s}^{-1}$ respectively.

dimensionless time is shown in figure 11 with data taken from Engel (1967), Morton *et al.* (2000) and two of the highest-momentum drops in this work. There is good agreement of the scaling with the data of Engel and Morton *et al.* during the growth period. The agreement is poorer during the early and late times of cavity formation. In the early stages, Cresswell & Morton (1995) have shown that vorticity is generated by drop impact and part of the energy of the impacting drop would have been lost during the vorticity generation process. After the early stage, the present analysis gives a good representation of the expanding cavity behaviour. The smallest drop studied generated by the 33G needle shows greater deviation with a curved line during the growth while the 16G needle drop has a central portion where it followed the $R'^{5/2}$ scaling. This is expected as the effect of surface tension was ignored, hence large drops with high impact momentum would follow the $R'^{5/2}$ scaling better than small drops. This is substantiated by the results of Engel where the momentum was substantially higher than achieved in this study. Photographs in Engel (1967) show that the cavity, formed by drops with a momentum much higher than achieveable in this study, are

https://doi.org/10.1017/S0022112000002500 Published online by Cambridge University Press

hemispherical. At late times, with the collapse phase being unstable, the scaling does not hold.

To obtain a scaling for the maximum cavity depth, the total energy available for the cavity growth process is assumed to be supplied by the kinetic energy of the drop ($\pi\rho_i d^3 u^2/12$). It is assumed that the cavity formed is hemispherical, which holds for high-momentum impacts and, hence, large *Fr* and *We* values. The surface tension energy is small compared to the kinetic energy of the drop, as represented by the inverse of *We*, and can be neglected. The potential energy of the cavity formed is given by $\pi\rho_t g R^4/4$. The energy balance gives

$$\frac{\pi R^4 \rho_t g}{4} + \pi\rho_t R^3 \left(\frac{\mathrm{d}R}{\mathrm{d}t}\right)^2 = \frac{\pi\rho_i u^2 d^3}{12}. \tag{3.11}$$

Rearranging equation (3.11), non-dimensionalizing the result, and integrating with respect to time gives

$$\int_0^{R'_m} (12\rho')^{1/2} \left(\frac{R'^3}{1 - 3R'^4\rho'/Fr}\right)^{1/2} \mathrm{d}R' = \int_0^{t'_m} \mathrm{d}t'. \tag{3.12}$$

Since *Fr* is large, the denominator is ≈ 1 and integrating gives $t'_m = (2/5)\sqrt{12\rho'}R_m'^{5/2} = 1.39\rho'^{1/2}R_m'^{5/2}$. Earlier, only 28% of the drop energy was found to be involved in the cavity formation. Using this fraction for the drop energy gives $t'_m = 2.62\rho'^{1/2}R_m'^{5/2}$.

Figure 12 shows dimensionless maximum cavity depth versus dimensionless time to reach maximum cavity depth for data obtained from the literature and this study. Engel (1966) provides data for large drops that are close to terminal velocity and Macklin & Metaxas's (1967) data include ethanol and glycerol drops impacting on the same target fluid. The 33G needle drops show much more deviation as the cavity depths often exhibited two maximums and the first maximum was chosen. This resulted in smaller times as the cavities were generally prolate in shape rather than hemispherical as assumed by the theoretical development. As the derivation is expected to fit the high-momentum impacts best, the data of Engel (1964) and Macklin & Metaxas (1976) were initially fitted with a power law curve giving $t'_m = 2.5R_m'^{2.45}$ with $r^2 = 0.98$. A least-squares fit to all the data for a power law curve gives $t'_m = 1.42R_m'^{2.84}$ with $r^2 = 0.97$. This indicates that for the lower momentum impacts less energy is lost during the formation of the cavity. As the deviation from the theoretical exponent is not too large, the complete set of data was refitted with the theoretical exponent to give $t'_m = 2.31R_m'^{2.5}$. The validity of the scaling was tested with a hypervelocity result of Gault reported by Holsapple & Schmidt (1987) for a Perspex sphere impacting onto a water target at 2500 m s^{-1} as shown in figure 12. The maximum cavity depth scaling with time obtained theoretically is able to cover the low to hypervelocity range ($R_m'^{5/2}$ from 0.5 to 10^4).

3.8. *The wave swell*

At low *We* and *Fr* (figure 2*a*, *b*), the wave swell is a capillary wave that expands outwards with time. Although not clear in figure 2, capillary waves can be seen propagating outwards ahead of the wave swell in figure 13. The steepness of the outward wave front decreases with time. The appearance of the steep wave front coincides with the appearance of the inward capillary wave travelling down the cavity wall (at 5 and 6 ms in figure 2*d*). When crown formation occurs, the appearance of the inward capillary wave is delayed and the outward travelling wave front has

https://doi.org/10.1017/S0022112000002500 Published online by Cambridge University Press

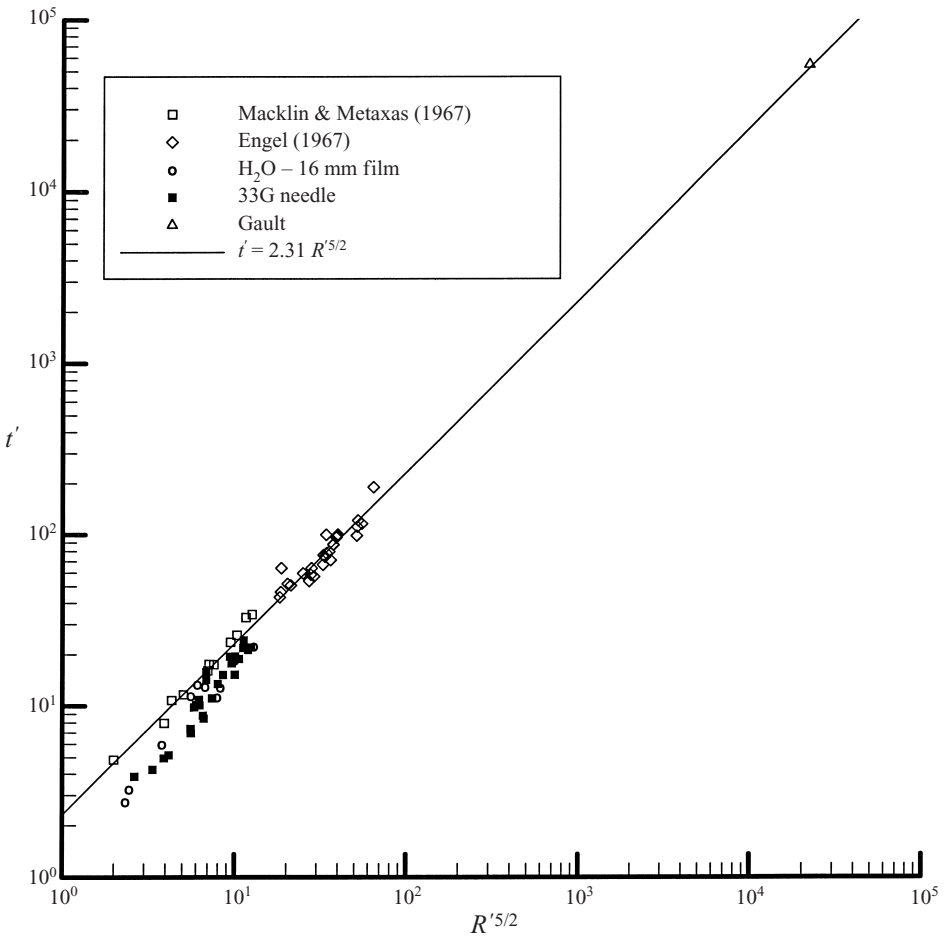


FIGURE 12. Variation of the dimensionless time required to reach dimensionless maximum cavity depth. The least-squares fit, without weighting, shifts the line in favour of the larger values. The smaller drops at low velocities give rise to cavity depths that do not increase monotonically with time and the time to the first maximum was chosen. Macklin & Metaxas's (1976) data include ethanol and glycerol runs. Engel (1964) used larger drops where the cavity depth expanded smoothly to the maximum cavity depth. The maximum experimental error is $t' = \pm 1$ for the experiments in this study.

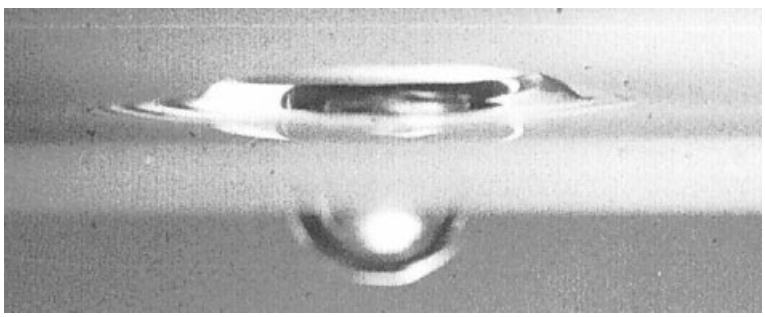


FIGURE 13. A top view of the early stages of cavity formation. Capillary waves can be seen propagating outwards ahead of the wave swell which has not yet collapsed.

https://doi.org/10.1017/S0022112000002500 Published online by Cambridge University Press

We	*Fr*	Average velocity of outward wave ($m\,s^{-1}$)	Average velocity of inward wave ($m\,s^{-1}$)
6.9	9.5	0.44	—
43	90	0.38	—
75	126	0.43	0.51
107	178	0.40	0.46
162	263	0.38	0.45
209	341	0.38	0.41
216	449	0.36	0.46
368	639	0.32	0.54

TABLE 3. Average velocities of the outward and inward travelling waves for the 33G needle drops. Inward travelling waves velocities are not measurable for low *Fr* and *We*.

already begun dissipating before the inward travelling wave can be seen on the cavity walls (figure 2*g*). The waves formed would be expected to consist of waves in a finite bandwidth (Longuet-Higgins 1990) and the long time behaviour of the impact area shows a clear region expanding outwards as the capillary waves have a finite minimum velocity (Crapper 1984). Linear plots obtained for the distance travelled by the outward and inward travelling waves against time indicated that the waves are travelling with a constant velocity. The measured velocities are given in table 3. The velocity of a capillary wave is given by $(2\pi\sigma/\lambda\rho)^{1/2}$. The velocity measured is higher than the minimum capillary wave velocity of $0.23\,m\,s^{-1}$. It is assumed that the capillary wave would be initially be a disturbance, and hence have a wavelength equal to the drop diameter. As pointed out in § 3.2.1, the inward travelling wave is a Crapper type wave with an amplitude of the order of the drop diameter.

The velocities of the outward travelling wave do not vary substantially for increasing *We* except for a small fall for *We* above 100. Crapper (1984) showed that the group velocity of a capillary wave is 3/2 times the phase velocity. The average velocity for the outward travelling waves is $0.38\,m\,s^{-1}$ which is about 10% higher than the minimum group velocity of $0.345\,m\,s^{-1}$. The outward travelling wave is initially propagating at close to the minimum group velocity for purely capillary waves before dispersion becomes significant. Measurements of the velocities of the outward travelling wave for the 16G drops over a number of different *We* between 70 to 300 also gave an average outward travelling wave velocity of $0.35\,m\,s^{-1}$.

3.9. *Upper limit to the high-speed jet regime*

OP(I) argued that the upper limit to the bubble entrapment regime occurs when the cavity grows radially when the drop material spreads evenly on the cavity surface. Morton *et al.* (2000) have confirmed numerically in the thick jet regime that the drop material does spread evenly on the cavity surface even though the cavity may not be growing hemispherically. The experiments show that the formation of the spray and crown marked the upper limit of the high-speed jet regime where the forces spreading the drop radially out overcome the surface tension forces. If so, $We \approx Fr^{1/4}$ should hold. Fitting the line to the experimental values in figure 1 gives $We = 54Fr^{1/4}$.

3.10. *Lower boundary for high-speed jet formation*

The experimental results show that the lower boundary for bubble entrapment is below the least-squares line of OP(I), which is $We = 41.3Fr^{0.179}$. Using the points

https://doi.org/10.1017/S0022112000002500 Published online by Cambridge University Press

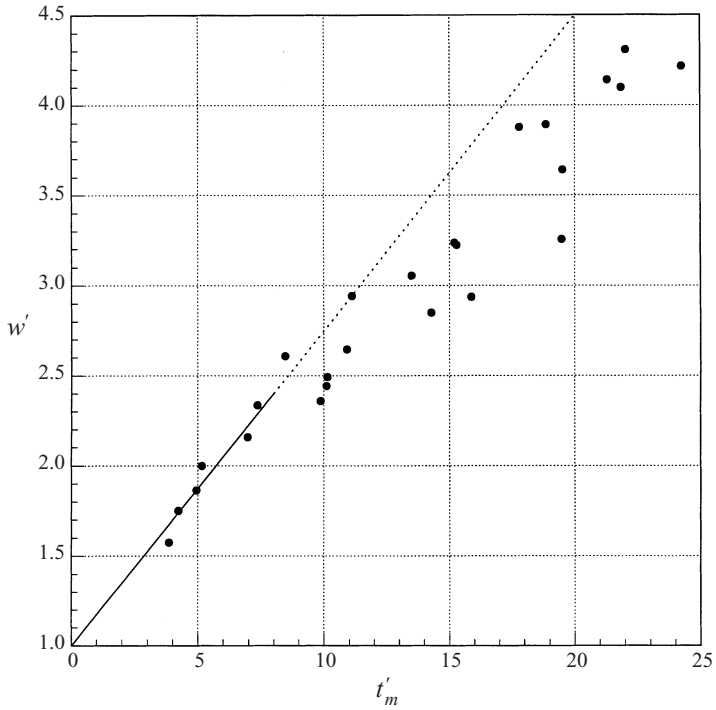


FIGURE 14. Variation of the dimensionless cavity width (measured as close as possible to the original undisturbed free surface position) reached at maximum cavity depth with dimensionless time to reach maximum cavity depth. The first six point are for low *We* and *Fr* in the regime of coalescence. The line of best fit is $w' = 1 + 0.175t'_m$. The other cases show a departure from the line as the cavity width takes longer to expand with time.

available for the 16G and 33G needle, the curve

$$We = 36.2Fr^{0.186} \tag{3.13}$$

is obtained. The lower boundary for the formation of a high-speed jet lies below the lower boundary for bubble entrapment. Using the points available for the 16G and 33G needle, the curve

$$We = 34.7Fr^{0.145} \tag{3.14}$$

is obtained as shown in figure 1. The *Fr* exponent is probably low since the experimental set-up limited the lowest *Fr* and *We* values attainable for the 16G runs.

Figure 14 shows the dimensionless cavity width reached at maximum cavity depth (w') against the dimensionless time to reach maximum cavity depth (t'_m). For the results in the bubble entrapment and thick jet regime, the cavity width (measured as close as possible to the original undisturbed free surface position) expands and contracts with the passage of the inward travelling waves at that point. The first six points in figure 14, for the results in the coalescing regime, fit a straight line passing though the drop diameter at impact time; thus w' varies linearly with t'_m. The variation of w' with t'_m can therefore be used as another parameter to detect the transition from the regime of coalescence to bubble entrapment.

The results for the splash–vortex ring boundary given by Rodriguez & Mesler (1985) with the mercury data of Hsiao *et al.* (1988) were shown in figure 1. A number of observations can be made. First, the data for the splash–vortex ring boundary

https://doi.org/10.1017/S0022112000002500 Published online by Cambridge University Press

coincide with the lower boundary for high-speed jet formation found in this study. Second, the results of Rodriguez & Mesler (1985) show an Fr dependence on We. This was not mentioned by Hsiao *et al.* (1988) and may have been overlooked since their definitions of Fr and We are the square root of the definitions used in this study which resulted in their plots being compressed. Third, the results suggest that there may not be a unique We value separating the splash–vortex ring boundary but rather the formation of the high-speed jet may disrupt the shedding of the large vortex ring seen by dyed drops. Instead, what was found previously was the lower boundary for high-speed jet formation. The value of $\sqrt{We} = 8$ to separate the splash–vortex ring boundary given by Hsiao *et al.* (1988) can be seen to be an averaged value for the data they had available.

4. Other observations

In some of the experiments, the drop detached from the Rayleigh jet did not rise far above the target liquid before falling back. This produced a wide range of small and large drops with low velocities which were captured on the film. The splash produced by these secondary drops covered much lower Fr and We values not easily generated experimentally. The positions of the drops on the (We, Fr)-plane are shown in figure 17 in § 5. These secondary drops may either bounce, coalesce with severe surface distortion, float on the target liquid surface, or exhibit a combination of these effects.

4.1. *Floating and bouncing drops*

Drops floating on the target liquid surface occurs only for Fr less than 7 and are clustered around the line $We = Fr$. Floating drops are rare and there is a dearth of data because the conditions for their formation occur in a small regime in the (We, Fr)-plane which is difficult to produce merely by dripping water from a nozzle. There are more data on bouncing drops in the literature. Bouncing drops are scattered over a wider range of Fr with $Fr > We$. The experimental data available suggest that for bouncing drops, We does not exceed 8 and the drops are smaller than 600 microns in diameter. Results for bouncing drops given by Rodriguez & Mesler (1985) and Ching, Golay & Johnson (1984) are included in figure 17. The boundary between floating and coalescing drops at present cannot be delineated based on experimental data. As the Fr increases, the drops coalesce with the target fluid without floating or bouncing. The data for the coalescing drops suggest that a similar line of the form $We = aFr$ can be used to separate the bouncing drop regime from the coalescing drop regime. A least-squares fit to the coalescing drops found in this study gives $We = 0.038Fr$. The regimes are delineated in figure 17. Two data points for coalescence with the formation of a cavity occur along the $We = Fr$ line when We is higher than 7. When compared with figure 1, the results indicate that drops having We larger than 8 would coalesce with cavity formation.

4.2. *Coalescence of floating drops*

Figure 15 shows the sequence in the coalescence of a large drop formed from a Rayleigh jet that has returned to the target liquid ($Fr = 6.6$, $We = 2.6$). The drop is highly distorted as it is still oscillating strongly due to the forces exerted during the breakup process. The drop impacts onto the crater still present in the target liquid. On impact, the drop flattens out and a sharp cusp is formed at its apex. Further flattening results in the cusp being smoothed out and the drop takes a flat tablet

https://doi.org/10.1017/S0022112000002500 Published online by Cambridge University Press

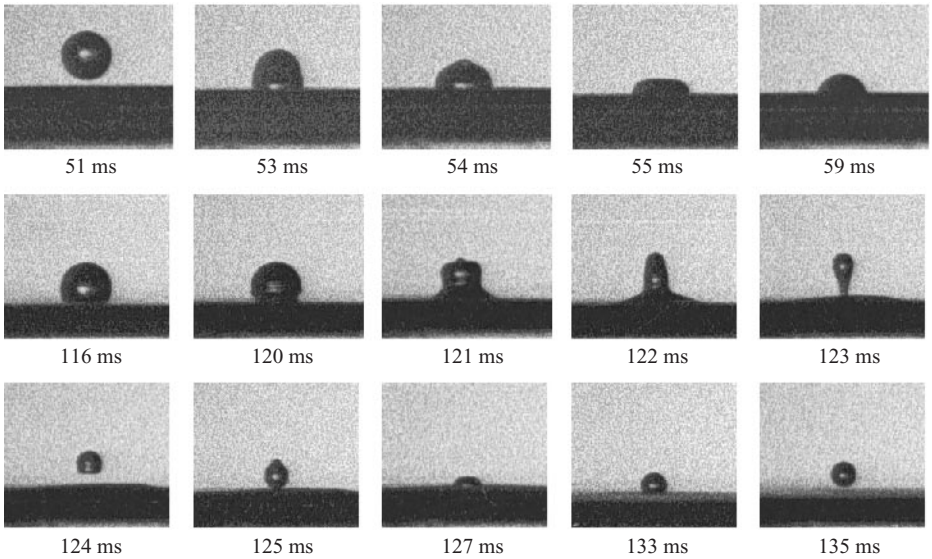


FIGURE 15. Coalescence of a floating drop with $Fr = 6.6$, $We = 2.6$, $d = 1.72$ mm and $u = 0.33\,\mathrm{m\,s^{-1}}$. The time in milliseconds is referenced to 0 ms for the frame just before drop impact for the first impacting drop at the start of the experiment.

shape. The tablet shape rebounds back to a spherical shape due to surface tension and oscillates slightly while resting on the surface. The drop floats on the target liquid surface for about 60 ms before coalescence takes place. During coalescence, a wave is created at the rim where coalescence occurs and the wave travels up the drop. In contrast, the target liquid surface is relatively undisturbed. MacKay & Mason (1963) showed experimentally that if the ratio of the diameters of two coalescing drops is greater than 12, the surface of the larger drop is undisturbed and can be treated as a flat surface. This criterion is applicable here. The propagating wave causes the drop to elongate into a stretched cylindrical column shape before a small drop of 0.76 mm diameter is ejected. This sequence is similar to the coalescence of water drops in silicone oil–CCl_4 solution shown in figure 11 of MacKay & Mason's (1963) paper. While the process took 25 ms in MacKay & Mason's experiment due to the higher viscosities of the liquids used, the process here takes only 4 ms. The pinched off drop is highly distorted and moves back towards the source of liquid. The drop does not coalesce but bounces off the target liquid. This is similar to observations by Zhang & Basaran (1995) for drops forming at a nozzle which they suggested were due to the unbalanced surface tension force on the thread during breakup. The thickness of the jet in the frame before breakup is 180 microns. For nozzles of similar diameter, Zhang & Basaran (1995) found that the satellite drops formed in their experiments moved towards the nozzle and then bounced off.

4.3. *Formation of small drops at the apex*

The formation of a small drop at the apex of an impacting drop was mentioned by Peck & Sigurdson (1994) for a drop of $Fr = 25 - 28$ and $We = 22 - 25$. Results to delineate the conditions for their formation are unavailable. Figure 16 shows the processes involved in the formation of an apex drop for the impact of a 2.3 mm drop at $0.47\,\mathrm{m\,s^{-1}}$ with $Fr = 9.5$ and $We = 6.9$. The apex drop does not pinch off. During impact, capillary waves are formed on the surface of the drop. These capillary

https://doi.org/10.1017/S0022112000002500 Published online by Cambridge University Press

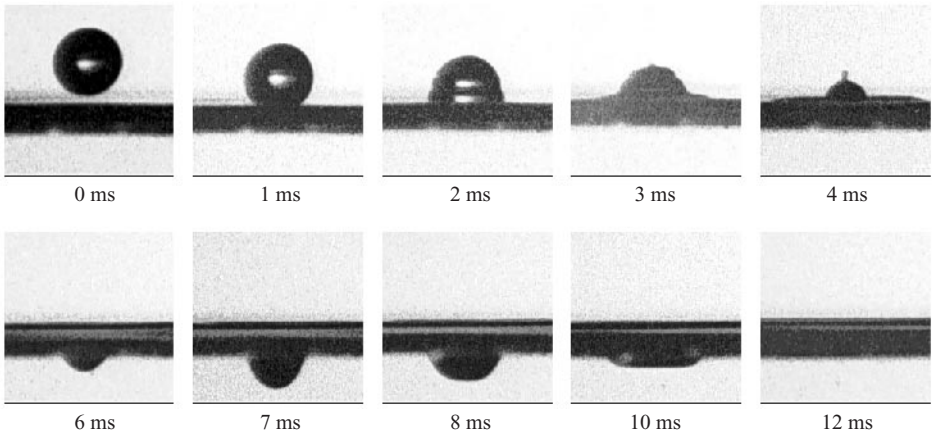


FIGURE 16. The formation of the apex drop for $Fr = 9.5$, $We = 6.9$, $d = 2.31$ mm and $u = 0.46\,\mathrm{m\,s^{-1}}$. In this case, the apex drop does not detach from the main drop.

waves are not seen in the photographs for drops at high Fr and We; the impacting drop surface is smooth. The surface waves propagate up towards the apex of the impacting drop and almost pinch off a small drop when about three quarters of the impacting drop has penetrated the target liquid. The impacting drop takes on a layered appearance with the formation of surface waves. A cavity is formed by the impacting drop. Despite the large range of results in this study, sighting of these apex drops is rare. However, when the condition for formation is suitable, the formation is repeatable. This was confirmed with a large number of drop impacts videotaped with a strobe at 300 flashes/s. It is also noted that the apex drops are not projected as splash drops above the free surface before the cavity has collapsed. Since the cavity does not form a jet, it is inferred that the apex drops adhere to the surface of the cavity and are ejected when the cavity collapses. Only one apex drop was observed to be formed.

5. Summary and conclusions

The impact of a spherical water drop onto a water target has been studied to provide qualitative and quantitative data. It is now possible to construct a much clearer picture of the variation of splash behaviour on the (We, Fr)-plane as given in figure 17. It shows for the first time that the primary bubble entrapment regime is a subset of the regime occupied by the high-speed jet. For water drops falling by gravity in air, the terminal velocity curve provides an envelope within which all the phenomena are found. The terminal velocity is calculated from the correlations given by Dingle & Lee (1972). Nevertheless, this picture is still not complete as much more data are required to fill in the surrounding regions. However, the important characteristics have been identified and the regions where they appear have been delineated.

For low We below 10, as the Fr increases, the phenomena observed begin with the impacting drop floating on the target liquid surface before coalescing later. As Fr is increased, the impacting drop bounces off the surface once or more times before coalescing. At even higher values of Fr and We up to the terminal velocity the impacting drops coalesce on impact with the target fluid.

https://doi.org/10.1017/S0022112000002500 Published online by Cambridge University Press

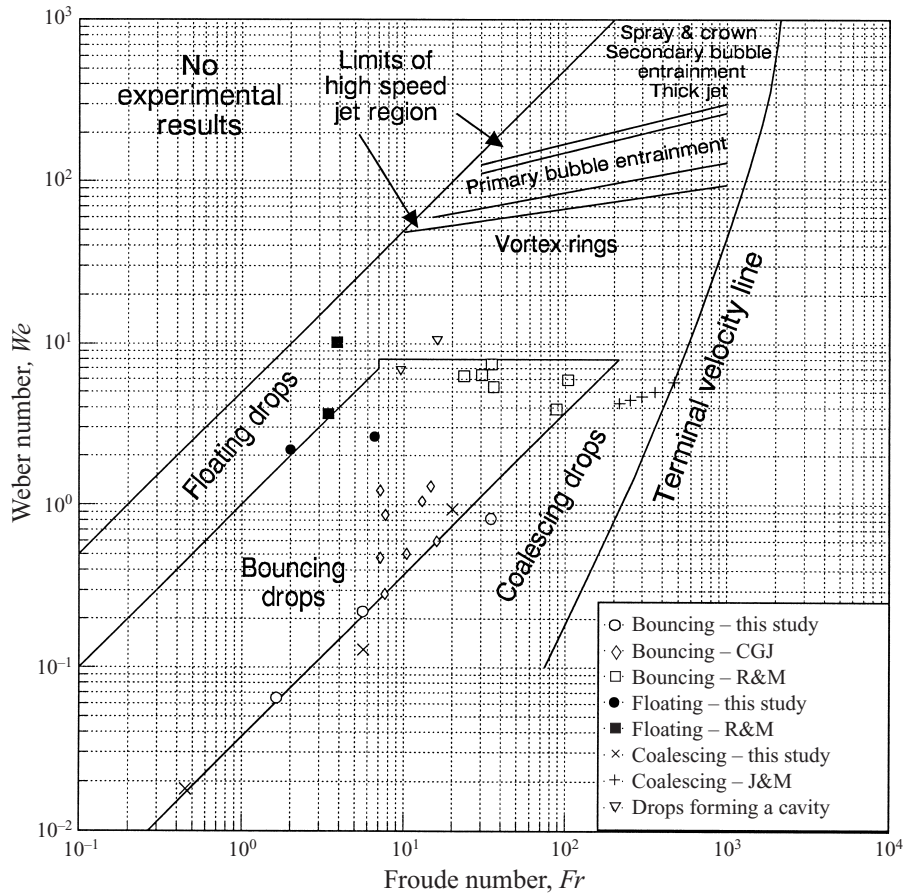


FIGURE 17. The We, Fr plot showing the different regimes. The approximate regimes for floating, bouncing or coalescing drops are separated by lines. The separation between the floating and coalescing regimes is still not well defined. The data are: CGJ, Ching *et al.* (1984), J & M, Jayaratne & Mason (1964), R & M. Rodriguez & Mesler (1985). The normal velocity component is used for drops impacting at an angle.

For We greater than 10, the impacting liquid drop phenomena studied hitherto including this study, are confined to a regime where $We/Fr < 5$ and within the terminal velocity line. As We is increased from 10, the impacting drop initially coalesces and vortex rings are propagated into the target liquid. In this coalescence regime, a capillary wave was found to move down the cavity sides and then converge towards the centre of the cavity with increasing aspect ratio. This capillary wave slows down the collapse of the cavity.

As We is increased, the capillary wave becomes steeper prior to the collapse of the cavity. This capillary wave is similar in profile to the Crapper wave. The trough at the centre becomes more pointed and it retracts to form a thin high-speed jet. The lower limit for the formation of the thin high-speed jet determined from experimental results is $We = 34.7Fr^{0.145}$. The lower limit for the formation of the thin high-speed jet was found to coincide with the splash–vortex ring boundary given by Rodriguez & Mesler (1965). It is postulated therefore that the lower limit for the formation of the high-speed jet and the splash–vortex ring boundary are identical. As We is increased

https://doi.org/10.1017/S0022112000002500 Published online by Cambridge University Press

further, the capillary wave becomes steep enough so that it entraps a bubble. Primary bubble entrapment occurs with the formation of a thin high-speed jet and the lower limit for primary bubble entrapment was determined as $We = 36.2Fr^{0.186}$. In the lower high-speed jet regime, the shape of the drop at impact can influence the cavity dynamics. Oblate impacting drops are less likely to result in a thin high-speed jet being formed for the 33G needle drops.

In the primary bubble entrapment regime, when the capillary wave moves down the sides of the cavity towards the base, the cavity wall moves inwards and then outwards relative to its centreline when the wave passes through. This is in contrast to the assumption that the cavity only expands and contracts once during its lifetime. The upper limit to the primary bubble entrapment regime was found to be close to the value of $We = 48.3Fr^{0.247}$ determined from experiments by OP(I). The thin high-speed jet was found to disappear at a slightly higher We and the upper limit to the high-speed jet regime was determined experimentally as $We = 54Fr^{0.25}$. The primary bubble entrapment regime was found to be a subset of the high-speed jet formation regime. It was also found that the upper limit for the high-speed jet formation coincides with the formation of a spray at the early stages of drop impact and the beginning of crown formation at the rim of the cavity.

Above the high-speed jet regime, the cavity forms a flat base before collapse and a thick jet is formed. The flat base of the cavity is irregular in shape and secondary bubble entrapment may occur from dimples in the cavity base. Larger drops were found to have the shape factor as an added parameter affecting the behaviour of splash formation in the high-speed jet and bubble entrapment regimes of the We, Fr plot. Although interesting it was not investigated as part of this study.

The equation for maximum cavity depth, (3.4) was found to be applicable to viscous liquids up to a viscosity of 3000 cP. How this is related to the drop impact Reynolds number is not known and will require further studies with viscous liquids. Equation (3.4) also indicates that only a quarter of the impacting drop kinetic energy is converted to the potential energy of the cavity. During the period of cavity growth where the kinetic energy of the liquid is large compared to the potential energy of the cavity, the dimensionless time for cavity growth scales according to $R'^{5/2}$. The dimensionless time to reach maximum dimensionless cavity depth R'_m was found to scale according to $R_m^{'5/2}$ and is valid over ten magnitudes of Fr. The wave swell travelling outwards was found to be travelling at close to the minimum group velocity for capillary waves.

The author would like to thank Dr M. Rudman for valued discussions. Financial support for this work was provided by the Australian Research Council and the Australian Government Cooperative Research Centres Program through the G. K. Williams Cooperative Research Centre for Extractive Metallurgy, a joint venture between the CSIRO Division of Minerals and the Department of Chemical Engineering, The University of Melbourne.

REFERENCES

Birkhoff, G. 1954 Note on Taylor instability. *Q. Appl. Maths* **12**, 306–309.

Cai, Y. K. 1989*a* Phenomena of a liquid drop falling to a liquid surface. *Exper. Fluids* **7**, 388–394.

Cai, Y. K. 1989*b* Collision of a water drop on water. *Acta Mechanica Sinica* **21**, 273–279 (in Chinese).

Chapman, D. S. & Critchlow, P. R. 1967 Formation of vortex rings from falling drops. *J. Fluid Mech.* **29**, 177–185.

https://doi.org/10.1017/S0022112000002500 Published online by Cambridge University Press

Ching, B., Golay, M. W. & Johnson, T. J. 1984 Droplet impacts upon liquid surfaces. *Science* **226**, 535–537.

Crapper, G. D. 1957 An exact solution for progressive capillary waves of arbitrary amplitude. *J. Fluid Mech.* **2**, 532–540.

Crapper, G. D. 1984 *Introduction to Water Waves*. Ellis Horwood.

Cresswell, R. W. & Morton, B. R. 1995 Drop-formed vortex rings – The generation of vorticity. *Phys. Fluids* **7**, 1363–1370.

Dingle, A.-N. & Lee, Y. 1972 Terminal fallspeeds of raindrops. *J. Appl. Met*. **11**, 877–879.

Edgerton, H. E. & Killian, J. R. 1954 *Flash.* Branford, Boston.

Engel, O. G. 1966 Crater depth in fluid impacts. *J. Appl. Phys.* **37**, 1798–1808.

Engel, O. G. 1967 Initial pressure, initial flow velocity, and the time dependence of crater depth in fluid impacts. *J. Appl. Phys.* **38**, 3935–3940.

Fink, J., Gault, D. & Greeley, R. 1984 The effect of viscosity on impact cratering and possible application to the icy satellites of Saturn and Jupiter. *J. Geophys. Res.* **89**, B1, 417–423.

Holsapple, K. A. & Schmidt, R. M. 1987 Point source solutions and coupling parameters in cratering mechanics. *J. Geophys. Res.* **92**, B7, 6350–6376.

Hsiao, M., Lichter, S. & Quintero, L. G. 1988 The critical Weber number for vortex and jet formation for drops impinging on a liquid pool. *Phys. Fluids* **31,** 3560–3562.

Jayaratne, O. W. & Mason, B. J. 1964 The coalescence and bouncing of water drops at an air/water interface. *Proc. R. Soc. Lond.* A **280,** 545–565.

Lawson, N. J. & Liow, J. L. 1998 Low cost design of 35 mm drum camera for high resolution, high speed image analysis. *Rev. Sci. Instrum.* **69,** 4195–4197.

Liow, J. L., Dickinson, W., Allen, M. & Gray, N. B. 1995 Study of slopping and splashing in a cylindrical bath with top submerged injection. *Metall. Mater. Trans.* **26B**, 887–889.

Liow, J. L. & Gray, N. B. 1996 Experimental study of splash generation in a flash furnace. *Metall. Mater. Trans.* **27B**, 633–646.

Longuet-Higgins, M. S. 1988 Limiting forms for capillary-gravity waves. *J. Fluid Mech.* **194**, 351–375.

Longuet-Higgins, M. S. 1990 An analytic model of sound production by raindrops. *J. Fluid Mech.* **214**, 395–410.

MacKay, G. D. M. & Mason, S. G. 1963 The gravity approach and coalescence of fluid drops at liquid interfaces. *Can. J. Chem. Engng* **41**, 203–212.

Macklin, W. C. & Metaxas, G. J. 1967 Splashing of drops on liquid layers. *J. Appl. Phys.* **47**, 3963–3970.

Morton, D. E., Rudman, M. & Liow, J. L. 2000 Bubble entrainment resulting from splashing drops. *Phys. Fluids* **12**, 747–763.

Oğuz, H. N. & Prosperetti, A. 1990 Bubble entrainment by the impact of drops on liquid surfaces. *J. Fluid Mech.* **219**, 143–179 (referred to herein as OP(I)).

Oğuz, H. N. & Prosperetti, A. 1991 Numerical calculation of the underwater noise of rain. *J. Fluid Mech.* **228**, 417–442.

Olevson, K. L. R. 1969 Energy balances for transient water cavities. *US Geol. Survey Prof. Paper* 650-D, pp. D189–D194.

Peck, B. & Sigurdson, L. 1994 The three-dimensional vortex structure of an impacting water drop. *Phys. Fluids* **6**, 564–576.

Prosperetti, A. & Oğuz, H. N. 1993 The impact of drops on liquid surfaces and the underwater noise of rain. *Ann. Rev. Fluid Mech.* **25**, 577–602.

Pumphrey, H. C. & Elmore, P. A. 1990 The entrainment of bubbles by drop impacts. *J. Fluid Mech.* **220**, 539–567.

Rein, M. 1996 The transitional regime between coalescing and splashing drops. *J. Fluid Mech.* **306**, 145–165.

Rodriguez, F. & Mesler, R. 1985 Some drops don't splash. *J. Colloid Interface Sci.* **106**, 347–352.

Rodriguez, F. & Mesler, R. 1988 The penetration of drop-formed vortex rings into pools of liquid. *J. Colloid Interface Sci.* **121**, 121–129.

Worthington, A. M. 1908 *A Study of Splashes.* Longmans, Green and Co.

Zhang, X. & Basaran, O. A. 1995 An experimental study of dynamics of drop formation. *Phys. Fluids* **7**, 1184–1203.

https://doi.org/10.1017/S0022112000002500 Published online by Cambridge University Press